Science Advances
AAAS

Supplementary Materials for

Engineered entropic forces allow ultrastrong dynamical backaction

Andreas Sawadsky *et al.*

Corresponding author: Warwick P. Bowen, w.bowen@uq.edu.au

Sci. Adv. **9**, eade3591 (2023)
DOI: 10.1126/sciadv.ade3591

This PDF file includes:

1 Supplementary files and scripts

Thermal equivalent circuit analysis script. This Mathematica notebook contains the data and code used to generate Fig. 2 of the main text, as well as Figs.S8, S9 and S10, using the thermal equivalent circuit analysis.

Additional simulation files and scripts are accessible from the Zenodo data repository at https://doi.org/10.5281/zenodo.6982289.

- This repository contains the Mathematica notebook containing the data and code used to generate Fig. 2 of the main text, as well as Figs.S8, S9 and S10. It can be found under: '\Zenodo repository\Thermal Circuit notebook\ThermalCalculationsMicroSphere_V12_AS.nb'
- This repository also contains the thermal, acoustic and optical COMSOL multiphysics simulation files used to generate Fig. 3b of the main text, as well as Figures S2, S3 and S6. These can be found under: '\Zenodo repository\Comsol simulations'

2 Experimental details

2.1 Experimental setup

The microsphere resonator is located in a superfluid-tight sample chamber at the bottom of a Bluefors dilution refrigerator (base temperature 10 mK) (*29*). Telecom laser light ($\lambda = 1554$ nm) from a low-noise erbium-doped fiber laser (Koheras ADJUSTIK) is evanescently coupled into the microsphere via a tapered optical fiber (*27*). Precise fiber positioning is achieved through Attocube nanopositioning stages. The measurements are performed with the pulse-tube cooler (PTC) turned off in order to minimize vibrations. When the PTC is switched off, substitute cooling power is provided by a liquid helium 'battery', containing approximately 1L of liquefied ^{4}He, located on the 4K stage, providing about 2-3 hours of measurement with the

pulse tube off. The sample chamber contains a small volume of alumina nanoparticles in order to increase the effective chamber surface area ($\sim$10 m^2), leading to more precise film thickness control and greater film thickness stability (*38*). While at base temperature, ^{4}He gas can be injected from the top of the cryostat into the sample chamber through a thin capillary, allowing for in situ control of the superfluid film thickness.

The microsphere resonator is obtained by melting the end of a silica single mode fiber (SMF-28) in a fusion splicer. The non-reflown end of the fiber is then held in place on a sample holder inside the cryostat by a large drop of UV glue. A scanning electron microscope image of three such resonators, of differing stem length l, is shown in Fig. S1. We employ Norland Optical Adhesive NOA 68 UV-curing glue for this purpose. This glue is chosen for its rapid curing time and relatively high viscosity (5000 cps). This allows for the glue to be cured before any wicking of the glue up the stem and onto the sphere itself which degrades its optical properties. This gluing procedure is robust to thermal cycling down to mK temperatures and the ensuing thermal stresses, likely due to large amount of glue used and the rough machined-aluminum sample holder surface providing an ample contact area for adhesion. In another context (fixing silica angle-polished fiber to smooth silicon, silica or HSQ-cladded wafers), the cryogenic survival of NOA 68 bonds was inferior, with a $>$90% failure rate after 5 thermal cycles. In that context, the use of an UV-curing glue containing a latent heat catalyst (NOA 86H from Norland Products) was found to provide superior performance. More details can be found reference (*61*).

2.2 Superfluid film thickness

The mean superfluid film thickness d_0 covering the microsphere resonator can be estimated by tracking the optical resonance frequency shift $\Delta\omega_0$ that a whispering gallery mode (WGM) experiences as a superfluid film forms onto the microsphere surface (*27, 29*). The film thickness d_0 is then given by $\Delta\omega_0/G$, with $G = \frac{\partial\omega_0}{\partial x}$ the optomechanical coupling rate which describes the

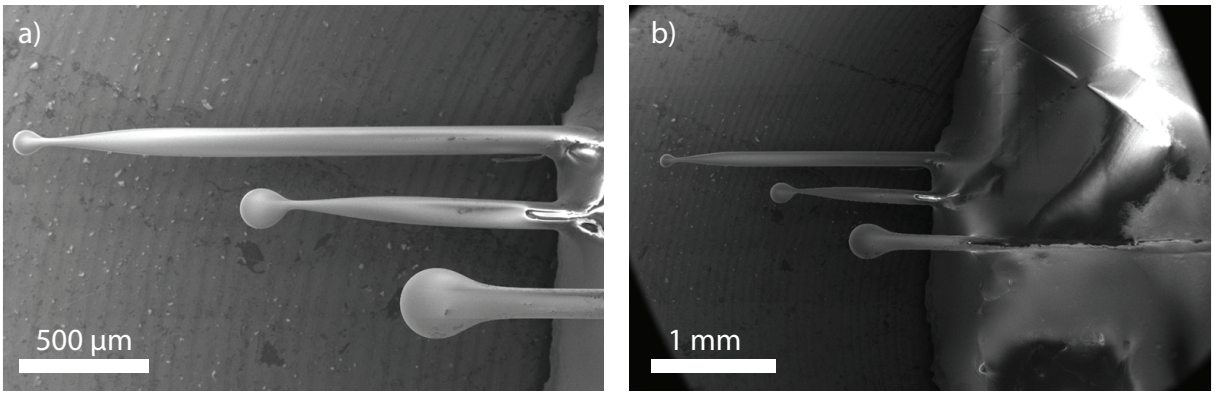

Figure S1: **Scanning electron micrographs.** Close-up (a) and large-scale (b) electron micrograph of three fabricated microspheres of differing stem length, held in place via UV-curing adhesive. The upper device was employed in the experiments. The white coloration in the UV glue is an artefact due to charging in the scanning electron microscope.

optical cavity angular resonance frequency shift per unit deposited superfluid film thickness on the resonator surface (*40*). Microsphere resonators support a wide variety of WGM resonances described by their radial, polar and azimuthal mode numbers along with their (TE or TM) polarization (*62*). However all these resonances have here a similar coupling strength G (see section 2.5), such that specific identification of the tracked WGM is not required.

An additional means to determine the film thickness is available for saturated films, as used in these experiments. As described above, the film is formed and thickened by injecting controlled volumes of ^{4}He gas into the sample chamber via a capillary. After a certain volume, any additional injected ^{4}He gas leaves the WGM resonance frequencies essentially unaffected. This corresponds to the regime of saturated film (*34, 63*), which differs from the unsaturated regime of our previous works (*27, 28, 32*). At this point the helium pressure in the chamber is equal to the saturated vapor pressure p_0, and any additional helium gas liquefies into a superfluid reservoir at the lowest point of the sample chamber. In this saturated regime, the film thickness is solely determined by the height z between the microsphere and the reservoir, and can be obtained by equating the van der Waals and gravitational chemical potentials $\mu_{\mathrm{vdW}} = \frac{-\alpha_{\mathrm{vdW}}}{d^3}$ and

$\mu_{\mathrm{grav}} = gz$, yielding (*34*):

$$d_0 = \sqrt[3]{\frac{\alpha_{\mathrm{vdW}}}{gz}} \tag{1}$$

Here $\alpha_{\mathrm{vdW}} = 2.6\times10^{-24}$ m^{5}s^{-2} is the van der Waals coefficient for silica (*40*) and $g = 9.8$ m.s^{-2} the gravitational acceleration. The latter method is for our system the most precise technique to determine the film thickness.

- The sphere is held at a height $z = 2$ cm +/- 1 mm above the lowest point in the sample chamber. In the saturated regime, Eq. (1) predicts a film thickness of $d_0 = 23.7$ nm +/- 0.4 nm.

- Using the WGM shift to determine the superfluid film thickness was less precise in these experiments. We observed an optical mode shift of 29 pm after a first helium injection. Using an optomechanical coupling rate $G/2\pi = 0.2$ GHz/nm (see section 2.5) this optical shift corresponds to a film thickness $d_0 = 18$ nm. Several days later we added more helium in order to better approach the experimental set-point shown in Fig. 2 of the main text and observed a mechanical mode frequency shift of 13 Hz, which suggest an additional film thickness of 2-3 nm, adding up to a total film thickness of $\simeq 21$ nm. Since these measurements were done over several days and combine two different techniques, this value has a larger uncertainty.

- A third option to determine the film thickness is using the eigenmode simulations in COMSOL. This is achieved by fitting the measured experimental frequency of the fundamental third sound mode (72 Hz), using the film thickness as fit parameter. This method leads to an estimated film thickness of $\sim$27 nm. This value has an uncertainty of around 3 nm, due to uncertainties in the exact length of the stem which defines the fundamental third sound mode (see section 2.3). The glue with which the stem is glued to the holder

could affect the length of the stem. A deviation of 400 μm could lead to a film thickness of 24 nm with matching frequency of 72 Hz.

Based on these calculations, we determine the superfluid film thickness to be 24 nm +/- 3 nm, which is within the error bars and agrees with all three thickness estimation methods.

2.3 Calculation of the third sound modes of the microsphere resonator

Previous experimental work with superfluid third sound resonators mainly employed disk-shaped resonators (*27–29, 38, 39*), for which analytical expressions (in the form of Bessel modes) exist for the third-sound resonances. While similar expressions exist for spheres (spherical harmonics), none naturally exist for the sound modes confined to the 2D outer surface of an arbitrary 3D geometry, such as the silica microsphere resonator including its supporting stem shown in the SEM micrograph in Fig. 3(a) of the main text. To address this, we note that the superfluid helium flow in the third sound wave is considered inviscid, irrotational and incompressible. (Indeed, while superfluid helium is in fact quite compressible (*64–66*) (with a bulk modulus of approximately 8 MPa compared to 2 GPa for water), the van der Waals pressure exerted on the superfluid helium's film free surface (typically in the kPa range for the film thicknesses considered here (*29*)) is approximately three orders of magnitude lower than helium's bulk modulus. As a consequence, any local influx of superfluid predominantly leads to a thickening of the film and not an increase in density, such that the superfluid may be well approximated as incompressible in the third sound wave). As such it is a potential flow and, in the limit of small wave amplitude, the out-of-plane deflection of the superfluid surface $\eta\left(\vec{r},t\right)$ obeys the simple wave equation:

$$\left(\nabla^2 - \frac{1}{c^2}\frac{\partial^2}{\partial t^2}\right)\eta = 0 \tag{2}$$

Here c is the speed of sound, which neglecting the influence of surface tension, takes the form $c_3 = \sqrt{3\frac{\rho_s}{\rho}\frac{\alpha_{\mathrm{vdW}}}{d^3}}$ (*40*). Assuming a separable time-harmonic standing wave solution, of the kind $\eta\left(\vec{r},t\right) = \eta\left(\vec{r}\right)e^{i\Omega t}$, leads to the Helmholtz equation for the spatial mode profile $\eta(\vec{r})$:

$$\left(\nabla^2 + k^2\right)\eta(\vec{r}) = 0, \tag{3}$$

where $k^2 = \frac{\Omega^2}{c^2}$ and the displacement profile $\eta(\vec{r})$ is defined on the (2D) surface of the (3D) resonator geometry. When the resonator is a sphere of radius R, the third sound modes are given by the eigenfunctions of the angular part of the Laplacian operator $\Delta = \nabla^2$, called the spherical harmonic functions $Y_m^l\left(\theta,\phi\right)$ of degree l and order m, with eigenvalue $k^2 = l(l+1)/R^2$ and frequency:

$$\Omega = kc = \frac{c\sqrt{l(l+1)}}{R}. \tag{4}$$

Similarly, the third sound modes confined to the surface of an arbitrary three dimensional geometry may be obtained through solving the Helmholtz equation on the exterior 2D surface of this 3D geometry with the help of finite element modelling software (Comsol Multiphysics). We use this technique to obtain the modes of oscillation of a superfluid film confined to the surface of a silica microsphere whispering gallery mode resonator, including its supporting stem.

Three such resonators, of differing stem length l, are shown in the top panel of Fig. S2(a), protruding from the sample holder in order to allow optical access through a tapered fiber (see bottom panel). Fig. S2(b) shows the fundamental mode of oscillation of a superfluid film confined to the surface of such a silica microsphere resonator. Acoustic confinement is provided by the large change in acoustic impedance at the contact point to the sample holder due to the rapid change in cross-sectional area, much like in a Helmholtz resonator (*67*). This is evidenced by the fact that the obtained resonance frequency $\Omega_M/2\pi =\sim 86\,\mathrm{Hz}$ for a 24 nanometer thick film—which reasonably closely matches that observed in the experiments—is essentially inde-

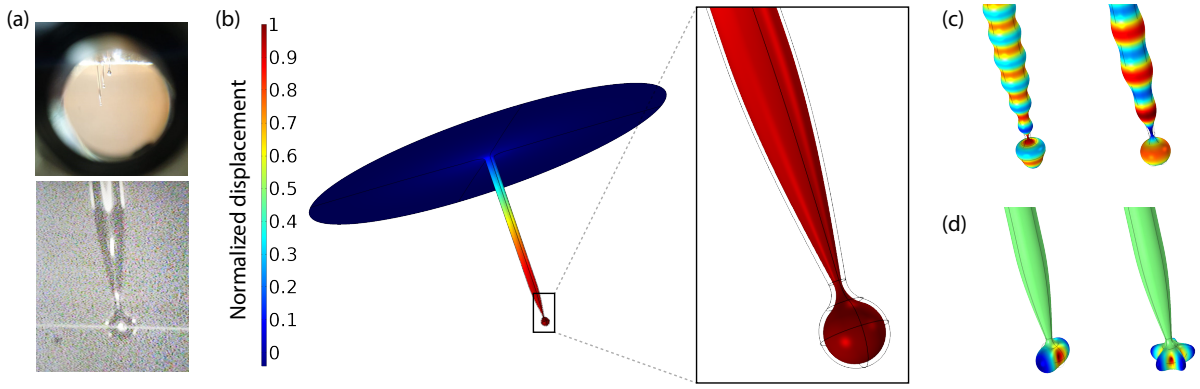

Figure S2: **Silica microsphere resonators.** (a) Top: three microspheres of varying diameter and stem length imaged through the sample chamber window. Bottom: image of the silica microsphere and the coupling tapered fiber, measured at cryogenic temperature with a long working distance microscope objective. (b) Fundamental third sound eigenmode localized to the fiber stem, obtained through finite element simulations. The rapid enlargement of the cross-section represents the point at which the fiber stem is glued to the sample holder. Inset shows how the fluid motion alternatively thins (and thickens) the film around the tip of the sphere. (c) Higher order third sound excitations of the fiber stem and microsphere. (d) Third sound modes localized to the microsphere tip, closely resembling the $Y_2^2(\theta, \phi)$ and $Y_5^5(\theta, \phi)$ eigenmodes of an ideal sphere.

pendent of the choice of fixed (Dirichlet) or free (von Neumann) boundary condition at the edge of the simulation domain (*40*). For this fundamental acoustic resonance, superfluid oscillates back and forth between the surrounding bath and the tip of the sphere, thereby efficiently modulating the whispering gallery mode optical path-length, as shown in the inset of Fig. S2(b). Higher order excitations of the stem and sphere are displayed in Fig. S2 (c).

This acoustic confinement through impedance mismatch is also at play at the level of the thin neck which joins the silica microsphere to the silica fiber stem. This results in (higher frequency) third sound modes localized on the spherical tip, as shown in Fig. S2(d), with mode profiles and eigenfrequencies closely matching those given by the spherical harmonic functions $Y_m^l(\theta, \phi)$ describing the eigenmodes of a perfect sphere (see section below).

Sphere modes

In addition to the fundamental stem mode discussed in the main text, we observe a number of high-frequency modes consistent with third sound modes localized on the microsphere itself. Fig. S3 shows a representative spectrum, acquired with a film thickness of ~ 7.5 nm. A number of third sound modes are visible with frequencies ranging from tens to hundreds of kHz and Q factors in the 10^4 range. These modes can be brought into regenerative oscillation with nanowatts of optical power. Which particular mode experiences dynamical backaction is strongly dependent on laser-cavity detuning. Fig. S3(b) records the frequencies of the third sound modes which could be brought into lasing during an experimental run. Both their density and frequency are consistent with spherical harmonics Y_m^l of an ideal sphere (pink bands, where l is incremented from 1 to 13). More precise mode identification was not performed here, as identifying the mode frequency provides information only on the degree l (see Eq. 4), and spherical harmonics of degree l have $2l+1$ degeneracy (the order m can take integer values from $-l$ to l). This is illustrated in the inset of Fig. S3(b), which displays the analytical spherical

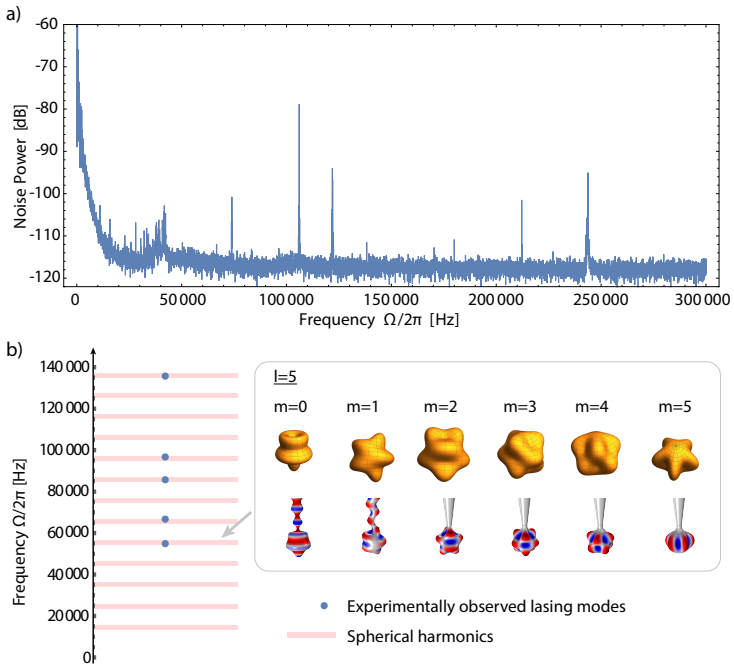

Figure S3: **Third sound modes localized on the microsphere.** (a) Power spectrum showing a number of high-frequency third sound modes, acquired with a film thickness of approximately 7.5 nm. (b) Matching of experimentally observed lasing modes (blue dots) to frequency of spherical harmonics Y_m^l of an ideal sphere (see Eq. (4)), (width of band 2 kHz).

harmonic modes of an ideal sphere $Y_m^l(\theta, \phi)$, along with the corresponding eigenmodes of the sphere with stem obtained through finite element simulation (negative values of m which rotate the eigenmode are not shown here).

2.4 Acoustic losses

2.4.1 Measurement of acoustic losses in the weakly pumped thermal Brownian motion regime

The intrinsic acoustic linewidth of the superfluid stem mode Γ is obtained by fitting the experimentally measured power spectral density below the threshold for regenerative oscillation, in the weakly pumped thermal Brownian motion regime. An example of this, measured with an incident power of 680 fW, is shown in Fig. S4. Accounting for the experimental uncertainty,

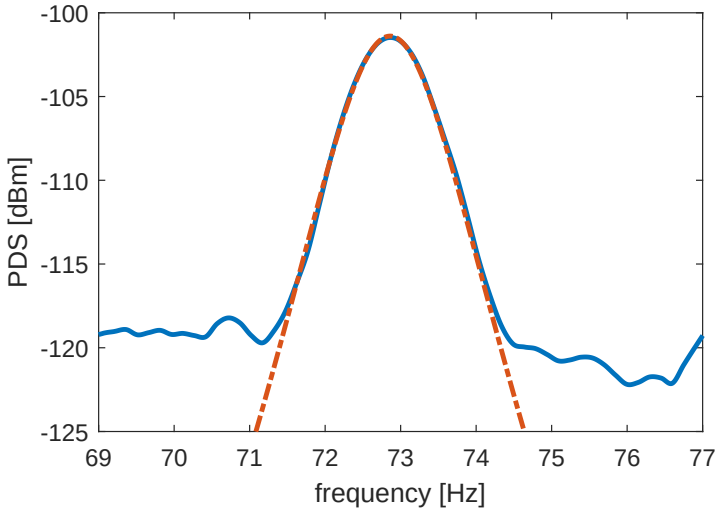

Figure S4: **Measurement of the stem mode acoustic linewidth.** Power spectral density (PSD) of the fundamental stem mode measured at an input power of 680 fW (blue), along with a lorentzian fit to the data (dashed red line). Accounting for uncertainty across repeated measurements, we extract an intrinsic damping rate $\Gamma/2\pi = 1.3 \pm 0.2$ Hz.

we extract an intrinsic loss rate $\Gamma/2\pi = 1.3 \pm 0.2$ Hz. As this value is close to the 1 Hz resolution bandwidth of our spectrum analyzer (Agilent N9010 EXA) , we corroborate it through an analysis of the superfluid acoustic losses in the following section.

2.4.2 Modelling the superfluid acoustic losses

In this section, we evaluate the acoustic losses of the superfluid stem mode discussed in the main text. We start by estimating the radiation-limit quality factor Q_{rad}. As mentioned above, acoustic confinement is provided by the large change in acoustic impedance at the contact point to the sample holder due to the rapid change in cross-sectional area, as illustrated in Fig. S1. This impedance mismatch reflects incoming superfluid waves, confining acoustic energy within the superfluid resonator. Since the contrast in acoustic impedances is finite, this reflection is only partial, and acoustic energy escapes the resonator, leading to acoustic losses, which play here the role of clamping losses in anchored mechanical resonators (*68*). These can be estimated

in a similar fashion to acoustic Helmholtz resonators in air (*69*).

To do this, we consider the superfluid wave shown in Fig. S5 (a), where the amplitude $\eta(x,t)$ takes the form $\eta = \eta_0 \cos(\omega t - kx)$. The energy per unit area carried by the wave under the form of kinetic and potential energy takes the form (*70*):

$$E = \frac{1}{2}\rho_{He} g_{\mathrm{vdw}}\, \eta_0^2, \tag{5}$$

in the limit of small amplitude. This result is identical to gravity waves, but the gravitational acceleration g has been replaced by the van der Waals acceleration of the substrate $g_{\mathrm{vdw}} = \frac{3\alpha_{\mathrm{vdW}}}{d_0^4}$. (We note that with our parameters $g_{\mathrm{vdw}} \simeq 2 \times 10^7$ m·s^{-2} $\gg$ g, which explains why gravity can be neglected in our experiments.) The power carried by the wave per unit length is given by E times the group velocity of the wave v_g. Third sound waves in superfluid helium are deep into the dispersionless shallow water wave limit ($d_0/\lambda \sim 10^{-5}$ here), such that $v_g = v_\phi = c_3$. The power carried by the wave is thus:

$$P = E v_g = \frac{1}{2}\rho_{He} g_{\mathrm{vdw}}\, \eta_0^2 c_3 \tag{6}$$

Figure S5 shows the normalized wave amplitude eigenmode profile obtained through finite element modelling as detailed in section 2.3. The amplitude is plotted as a function the the arc length highlighted in the inset, where the '0' coordinate corresponds to the tip of the microsphere. Due to the finite impedance mismatch there is a finite motion of the superfluid film at the level of the 'neck' of the superfluid Helmholtz resonator, materialized by the red dot. This launches a wave with power $\frac{1}{2}\rho_{He} g_{\mathrm{vdw}}\, \eta_0^2 c_3$ into the environment. The radiative quality factor Q_{rad} is defined as 2π times the ratio between the total energy stored in the system W and the radiative energy lost during one cycle of oscillation at resonance ΔW_{rad} (*68*):

$$Q_{\mathrm{rad}} = 2\pi \frac{W}{\Delta W_{\mathrm{rad}}} \tag{7}$$

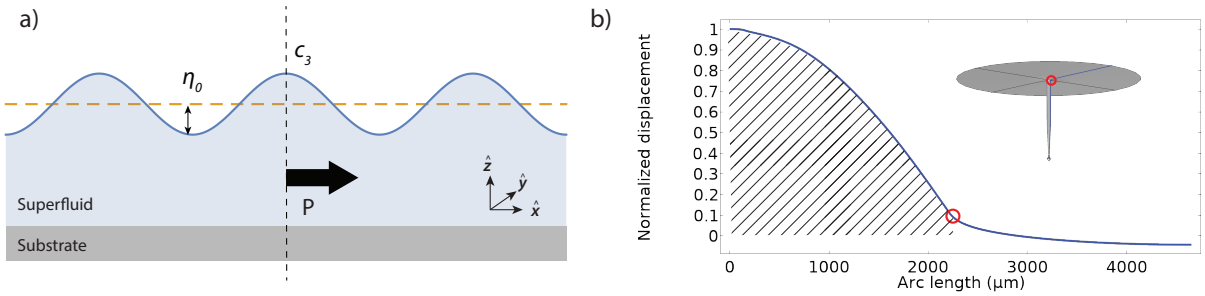

Figure S5: **Modelling the superfluid acoustic losses.** (a) Cross-section of a superfluid third sound wave, showing the wave amplitude η_0 and the phase/group velocity c_3. The power P per unit length (along the $\hat{y}$ direction) carried by the wave through the dashed black line is given by (6). (b) Finite element simulation of the stem mode normalized displacement (see Fig. S2(b)), with the displacement at the level of the 'neck' of the resonator highlighted by the red circle.

Substituting into (7) the values of W and $W_{\rm rad}$ obtained through Eqs.(5) and (6), we get:

$$Q_{\rm rad} = \frac{2\pi f}{c_3} \frac{\iint_{\rm res.} \eta^2(\vec{r})\, {\rm d}A}{\int_{\rm circ.} \eta^2\,(\vec{r})\, {\rm d}l}, \tag{8}$$

where the numerator integral is carried over surface area of the resonator (silica sphere+stem), while the denominator integral is carried over the circumference of the neck of the resonator through which power flows into the environment. Using the results of the finite element modelling, Eq. (8) provides an estimate for the radiative decay rate $\Gamma_{\rm rad} = \Omega/Q_{\rm rad}$. We find $\Gamma_{\rm rad}/2\pi = 1.5$ Hz.

Unambiguous identification of all damping mechanisms in third sound remains an open problem in the field. The main known dissipation channels include thermal dissipation arising due to the temperature gradient between the peaks and troughs of the sound wave, dissipation due to interactions with pinned vortices, and radiation losses (*71*). The total quality factor $Q_{\rm tot}$ is then related to the individual quality factors by $Q_{\rm tot}^{-1} = Q_{\rm rad}^{-1} + Q_{\rm other}^{-1}$. Given the over two orders of magnitude larger Q factors measured on the sphere modes, which are better confined to the extremity of the microsphere (see section 2.3), it is reasonable to assume that radiative losses are the dominant source of loss for the stem mode, such that $\Gamma_{\rm rad} \simeq \Gamma_{\rm tot}$, in good agreement

with the experimentally measured values discussed in the previous section.

2.5 Calculation of effective mass, coupling rate and thermal conductance

Optomechanical coupling G

Calculating the optomechanical coupling G requires identification of the employed WGM in order to compute its field overlap with the superfluid coating the resonator (*40*). However, microspheres have a very dense whispering gallery mode spectrum, with WGMs differing by their radial, polar and azimuthal mode orders (n, l and m respectively), along with their TE or TM polarization (*62*), as illustrated in Fig. S6(a). This large WGM mode density makes it difficult to identify the mode used in the experiments. Fortunately, changes in the WGM order have only a modest influence on the coupling strength, with a $< 1\%$ change arising from incrementing the radial or polar order beyond the fundamental mode (see Fig. S6(a)).

A larger difference, on the order of 5%, arises between TE and TM polarizations. Indeed, the WGMs with a dominant radial E field component have a larger field at the surface due to the orthogonal E field discontinuity at the silica interface (*40*). Calculation for 100 WGMs closest in resonance wavelength to 1550 nm shows that their G is bounded between 1.9×10^{17} and 2.1×10^{17} Hz/m, allowing us to constrain the uncertainty to within $\sim$10%. These calculated values are in good agreement with the analytical expression for a circular WGM resonator $G = -\frac{\omega_0}{R}$ (*72*), corrected for the lower dielectric permittivity of superfluid helium (*40*):

$$G = \frac{\partial \omega_0}{\partial x} \simeq -\frac{\omega_0}{R}\left(\frac{1-\varepsilon_{\mathrm{sf}}}{1-\varepsilon_{\mathrm{SiO_2}}}\right), \tag{9}$$

which predicts $G/2\pi = 1.93 \times 10^{17}$ Hz/m for a 55 μm radius sphere. Here $\varepsilon_{\mathrm{sf}} = 1.058$ is the relative permittivity of superfluid helium (*73*), and $\varepsilon_{\mathrm{SiO_2}} = 2.1$ that of silica. We note the value of G is calculated with a radius of 55 μm, obtained by an optical microscope measurement. Elsewhere a value of 49.5 μm obtained by SEM is used. This discrepancy is due to the oblate shape of the reflown microsphere.

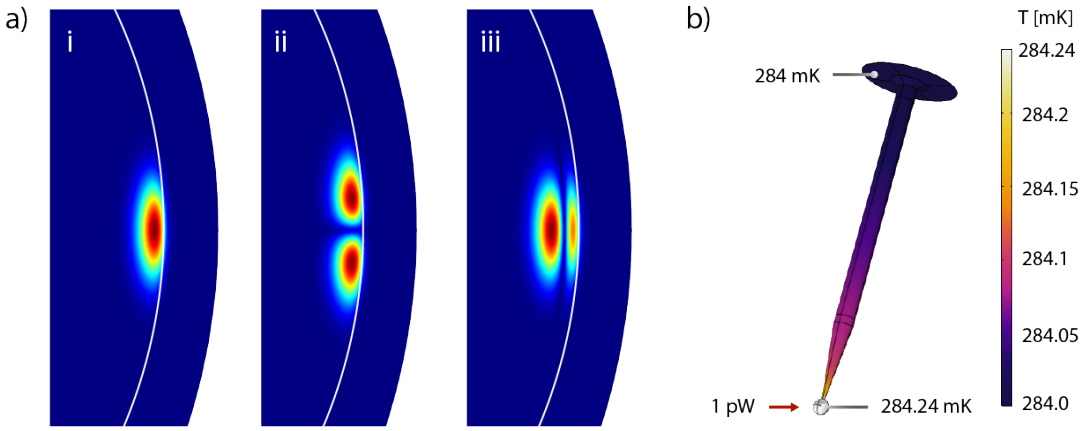

Figure S6: **Optomechanical coupling and thermal conductance.** (a) Whispering gallery modes of a 55 μm radius microsphere resonator, obtained through finite element simulation. i) Fundamental radial $n = 1$ and polar $l = 1$ WGM with azimuthal number $m = 320$ and resonance wavelength $\lambda_0 = 1506$ nm. Its optomechanical coupling strength calculated through FEM (*40*) is $G/2\pi = 1.883 \times 10^{17}$ Hz/m. ii) Higher order polar WGM ($n = 1$; $l = 2$; $m = 320$), with optomechanical coupling strength $G/2\pi = 1.889 \times 10^{17}$ Hz/m. iii) Higher order radial WGM ($n = 2$; $l = 1$; $m = 320$), with $G/2\pi = 1.903 \times 10^{17}$ Hz/m. (b) Calculation of the thermal conductance of the microsphere resonator. An absorbed power of 1 pW at the level of the spherical tip leads to a steady-state temperature increase by 0.24 mK, corresponding to a thermal conductance $G_{\rm th} = 4.1 \times 10^{-9}$ W/K at a thermal bath temperature of 284 mK. Physical parameters used in the simulation are summarized in Table S3.

Effective mass

The effective mass of an acoustic mode taken at a reduction point $\vec{R}$ is obtained by reducing the system to a point mass m_{eff} moving with velocity $v(\vec{R})$ possessing the same kinetic energy E_k as the original system, that is $m_{\text{eff}} = \frac{2E_k}{v(\vec{R})^2}$. For a third sound mode, this takes the form (*40*):

$$m_{\text{eff}} = \frac{2E_p}{v^2(\vec{R})} = \frac{2\iint \frac{3\rho\alpha_{\text{vdW}}\eta^2(\vec{r})\mathrm{d}^2(\vec{r})}{2d^4}}{\eta^2(\vec{R})\,\Omega^2}, \tag{10}$$

where $E_p = E_k$ is the potential energy stored in the third sound wave, and the integral is taken over the surface $\mathcal{A}$ of the resonator. For the fundamental mode of the sphere and stem shown in Fig. S2(b), with a reduction point on the equator of the microsphere and a 24 nm film thickness, $m_{\text{eff}} = 5.1 \times 10^{-3}$ kg. Note that this value is approximately 2 billion times larger than the total mass of superfluid covering the resonator $m = \mathcal{A}\, d\, \rho_{\text{He}} = 2.65 \times 10^{-12}$ kg. The larger effective mass arises from the fact we consider here only the out-of-plane displacement η of the fluid interface (which couples to the light), while the majority of the superflow occurs in plane (*40*).

Radiation pressure Single photon optomechanical coupling rate $g_{0_{rp}}$

For the low-frequency stem mode shown in Fig. S2(b), the superfluid displacement is uniform along the tip of the microsphere where the light is confined, such that the radiation pressure single photon optomechanical coupling rate $g_{0_{rp}}$ is given by (*10, 40*):

$$g_{0_{rp}} = G x_{\text{zpf}} = G\sqrt{\frac{\hbar}{2m_{\text{eff}}\Omega}}. \tag{11}$$

With $G/2\pi = 2 \times 10^{17}$ Hz/m (see section 2.5) and $m_{\text{eff}} = 5.1 \times 10^{-3}$ kg (see section 2.5), this yields $x_{\text{zpf}} = 4.8 \times 10^{-18}$ m and $g_{0_{rp}}/2\pi = 0.95$ Hz.

3 Thermal-electric circuit analogy

The fountain pressure in superfluid helium is given by (*33*):

$$P_{\mathrm{fp}} = \rho_{\mathrm{He}}\, S_{\mathrm{He}}(T)\, \Delta T_{\mathrm{He}}, \tag{12}$$

where ρ_{He} is the superfluid helium density, $S_{\mathrm{He}}(T)$ is the temperature-dependent entropy of helium, and $\Delta T_{\mathrm{He}} = T_{\mathrm{He}} - T$ is the difference between the environment temperature T and the superfluid film covering the resonator at temperature T_{He}. When calculating the fountain pressure force the challenge is to precisely estimate the temperature rise in the superfluid film, because it strongly depends on the thermal parameters of the system (thermal conductivity, specific heat, Kapitza resistance, vapor pressure etc), which in turn are all strongly temperature-dependent. To model this system we use the technique of the thermal-electric analogy.

The thermal-electric analogy as a lumped-element model is a well known approach to analyse and simulate a variety of complex thermal systems (*74, 75*). Applications of thermal equivalent circuits range from designing heat sinks for semiconductor circuits (*76*) and understanding the impact of solar radiation on building energy consumption (*77*) to battery pack thermal management (*78*). Here we use the analogy between thermal quantities and electric quantities (summarized in Table S1) to transform our thermal system into an electric circuit analog. In figure S7 a) we show a schematic of our thermal system with the equivalent electric quantities and in b) the electric circuit as an analog representation of our thermal system. The heat source in our system is the absorbed intracavity optical power in the silica sphere, which is represented by the current source I_{ph} in the circuit. There are two paths for the heat flow towards the thermal bath (dark grey). First it can flow through the substrate itself, i.e. the silica stem which is thermally anchored to the cryostat (beige colored area). Second it may flow through the silica/superfluid interface (striped line) with interfacial resistance R_K into the superfluid helium (light blue color) and dissipate via evaporation. Because the heat can dissipate through

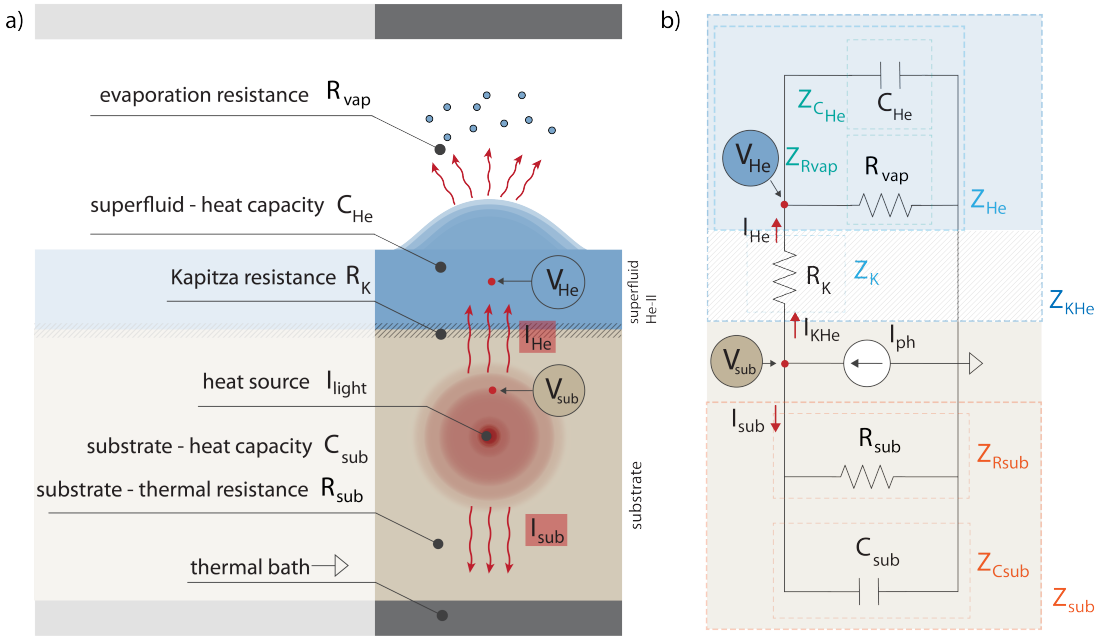

Figure S7: **Electric-thermal analogy scheme.** a) shows the schematic of our thermal system with the analog electric quantities. The analogy for the heat source (absorbed intra cavity power) is a current source I_{light} and the electric ground represents the thermal bath of the system. b) Electric circuit analogy of our thermal system. The voltages V_{sub} and V_{He} are the analogs of the temperatures in the substrate and the superfluid film.

electric	thermal	superfluid mass flow
charge $q[A \cdot s]$	heat $Q[J]$	mass $m[kg]$
current $I[A]$	heat flow rate $\dot{Q}[W]$	mass flow rate $\dot{m}[kg/s]$
voltage $V[V]$	temperature $T[K]$	chemical potential $\mu[J/kg]$
resistance $R[V/A]$	heat resistance $R_{\mathrm{th}}[K/W]$	-
capacitance $C[A \cdot s/V]$	heat capacitance $C_{\mathrm{th}}[J/K]$	mass capacitance $C_{\mathrm{m}} = dm/d\mu[1/J]$
inductance $L[H]$	-	mass inductance $L_{\mathrm{m}}[m^2/kg]$
$I = \Delta V/R$	$\dot{Q} = \Delta T/R_{\mathrm{th}}$	-
$I = CdV/dt$	$\dot{Q} = C_{\mathrm{th}}dT/dt$	$\dot{m} = C_{\mathrm{m}}d\mu/dt$
Kirchoff's current law	first law of thermodynamics	law of conservation of mass

Table S1: **Electric, thermal and superfluid mass flow analog quantities.**

both paths simultaneously, these are arranged in parallel in the electric circuit. The two main quantities we are interested in are the temperature changes in the substrate ΔT_{sub} and in the superfluid helium thin film ΔT_{He} with respect to the thermal bath. These two quantities are represented by the two thermal potentials (electric analogy: voltage) V_{sub} and V_{He} with respect to some reference voltage, which is the thermal bath (electric analogy: ground). They depend on the thermal resistances R_{th}, capacitance C_{th}, thermal bath temperature T and heat flow rate given by the absorb photons, which is the current I_{ph} in the electric analogy. Knowing these values, we eventually can calculate the fountain pressure and force.

3.1 Thermal-electric elements of substrate - silica

In a lumped-element model for heat transfer an element with a non-zero heat capacity is is modeled by two quantities in a parallel configuration: a thermal resistance $R_{\mathrm{th-sub}}$ and a thermal capacitance $C_{\mathrm{th-sub}}$ which accounts for the element's thermal inertia.

The thermal resistance R_{sub} can be simulated with COMSOL. All parameters used in this simulation are provided in Table S3 and are for the bath temperature of 284 mK. Fig. S6(b) shows the steady-state temperature increase in the microsphere plus stem system with $\dot{Q} = 1$ pW of optical power absorbed at the level of the microsphere. The 0.24 mK temperature in-

crease corresponds to a thermal resistance $R_{\mathrm{th-sub}} = 2.44 \times 10^8\,\mathrm{K/W}$ and a thermal conductance $G_{\mathrm{th-sub}} = R^{-1}_{\mathrm{th-sub}} = \kappa_{\mathrm{SiO_2@284mK}} \times \phi = 4.1 \times 10^{-9}\,\mathrm{W/K}$, where $\kappa_{\mathrm{SiO_2@284\,mK}} = 1.6 \times 10^{-3}\,\mathrm{W/m/K}$ is the thermal conductivity for silica at 284 mK and $\phi = 2.52 \times 10^{-6}\,\mathrm{m}$ is a temperature-independent geometrical factor (which we obtain from this simulation). The thermal conductivity of silica $\kappa_{\mathrm{SiO_2}}(T)$ is temperature dependent. In figure S8 a) we fitted a function of the form $\kappa_{\mathrm{SiO_2}}(T) = 0.0000488638 \times T + 0.0212904 \times T^2 - 0.00436582 \times T^3 - 0.000101651 \times T^4$ to the data from (*79*) to get a temperature-dependent thermal resistance of the silica microsphere $R_{\mathrm{th-sub}}(T) = (\kappa_{\mathrm{SiO_2}}(T) \times \phi)^{-1}$.

The thermal capacitance of the substrate is given by $C_{\mathrm{th-sub}} = c_{\mathrm{SiO_2}}(T) \times m_{\mathrm{sub}}$, with m_{sub} being the mass of the microsphere (incl. stem) and $c_{\mathrm{SiO_2}}(T) = 0.00105 \times T + 0.0018 \times T^3$ is the temperature-dependent specific heat capacity for silica (see figure S8 b)), which is a fit function to the data from (*80*).

3.2 Thermal Kapitza resistance at the interface

The interface between the silica and the superfluid thin-film results in an interfacial thermal resistance called the Kapitza resistance. It is temperature and material dependent, and arises due to the large acoustic impedance mismatch between silica and superfluid helium, reducing phonon propagation from one medium to the other. According to (*81*) the Kapitza resistance has the functional form:

$$R^{'}_{\mathrm{K}}(T) = \frac{15\hbar^3 \rho_{\mathrm{SiO_2}} c^3_{t_{\mathrm{SiO_2}}}}{2\pi^2 k^4_{\mathrm{B}} \rho_{\mathrm{He}} c_{1_{\mathrm{He}}} F(\frac{c_{l_{\mathrm{SiO_2}}}}{c_{t_{\mathrm{SiO_2}}}}) T^3}, \tag{13}$$

where $\rho_{\mathrm{SiO_2}}$ and ρ_{He} are the densities of silica and liquid helium, $c_{t_{\mathrm{SiO_2}}}$ and $c_{l_{\mathrm{SiO_2}}}$ are respectively the transverse and longitudinal sound velocities of silica, $c_{1_{\mathrm{He}}}$ is the first sound speed in superfluid helium and $F(c_{l_{\mathrm{SiO_2}}}/c_{t_{\mathrm{SiO_2}}}) = 2.5$ (*81*) is a silica specified function. Fig. S8(c) shows the temperature dependency of the Kapitza resistance for a silica and superfluid helium interface

with units $[\mathrm{m^2K/W}]$. When calculating the Kapitza interfacial thermal resistance in our system R_{K}, we need to normalize it to the silica microsphere surface area, i.e. $R_{\mathrm{K}}(T) = R'_{\mathrm{K}}(T)/\mathcal{A}$ [K/W].

3.3 Thermal-electric elements of superfluid helium He-II

The superfluid helium thin-film is represented by the thermal resistance R_{vap} and the thermal capacitance C_{He}. In thin superfluid films, the normal fluid component is viscously clamped to the substrate and does not flow. Only the superfluid component, which carries no entropy, is free to move. Thermal conductance through the liquid itself is therefore negligible, and the thermal conductivity occurs primarily through influx of superfluid, which evaporates extracting the latent heat of vaporization (*82*). To calculate the thermal conductance $G_{\mathrm{vap}}(T)$ resulting from this evaporative process at a temperature T, we need to multiply the resulting net helium mass flow rate per unit area $\dot{m}_{\mathrm{He}}$ by the latent heat of vaporization of helium $L_{\mathrm{He}(T)}$ and divide by the temperature change $(T_0 - T)$, which gives the area-normalized 'net' energy leaving due to evaporation. Multiplying by the silica microsphere area $\mathcal{A}$ gives the total evaporative thermal conductance of our superfluid film:

$$G_{\mathrm{vap}}(T) = \dot{m}_{\mathrm{He}} \frac{L_{\mathrm{He}}(T)}{(T_0 - T)} \mathcal{A}. \tag{14}$$

The net mass flow rate per unit area is given by (*25*):

$$\dot{m}_{\mathrm{He}}(T) = \gamma \sqrt{\frac{m_{\mathrm{He_{mol}}}}{2\pi R\, T}} \left(\frac{dP_{\mathrm{V}}}{dT}\right)_{\mathrm{v.p.c}} (T_0 - T), \tag{15}$$

with $\gamma = 1$, $m_{\mathrm{He_{mol}}}$ as the molar mass of helium, $R = 8.3145$ J mol^{-1} K^{-1} the ideal gas constant and $(\frac{dP_{\mathrm{V}}}{dT})_{\mathrm{v.p.c}}$ the gradient of the vapour pressure curve for helium. The saturated vapour pressure $P_{\mathrm{V}}(T)$ curve is plotted in Fig. S8(e), and given by (*73*):

$$P_{\mathrm{V}}(T) = \exp(i_o - \frac{L_0}{RT} + \frac{5}{2}\log(T)), \tag{16}$$

Thermal-electric quantity	functional form	frequency domain
Substrate thermal resistance	$R_{\mathrm{sub}}(T) = (\kappa_{\mathrm{SiO_2}}(T)\phi)^{-1}$	$Z_{\mathrm{R_{sub}}}(T) = R_{\mathrm{sub}}(T)$
Substrate thermal capacitance	$C_{\mathrm{sub}}(T) = c_{\mathrm{SiO_2}}(T) m_{\mathrm{sub}}$	$\tilde{Z}_{\mathrm{C_{sub}}}(\Omega, T) = \frac{1}{i\Omega C_{\mathrm{sub}}(T)}$
Kapiza Resistance	$R_{\mathrm{K}}(T) \simeq \frac{3\hbar^3 \rho_{\mathrm{SiO_2}} c_{t_{\mathrm{SiO_2}}}^3}{\pi^2 k_{\mathrm{B}}^4 \rho_{\mathrm{He}} c_{1_{\mathrm{He}}} T^3 \mathcal{A}}$	$Z_{\mathrm{K}}(T) = R_{\mathrm{K}}(T)$
Superfluid He thermal resistance	$R_{\mathrm{vap}}(T) = \left(\gamma \sqrt{\frac{m_{\mathrm{He_{mol}}}}{2\pi RT}} (\frac{dP_{\mathrm{V}}}{dT})_{\mathrm{v.p.c}} L_{\mathrm{He}}(T) \mathcal{A}\right)^{-1}$	$Z_{\mathrm{R_{vap}}}(T) = R_{\mathrm{vap}}(T)$
Superfluid He thermal capacitance	$C_{\mathrm{He}}(T) = c_{\mathrm{He}}(T) m_{\mathrm{He}}$	$\tilde{Z}_{\mathrm{C_{He}}}(\Omega, T) = \frac{1}{i\Omega C_{\mathrm{He}}(T)}$

Table S2: **Thermal-electric quantities in DC and frequency domain.**

where $i_0 = 12.2440$ and $L_0 = 59.83$ J/mol is the latent heat of vaporization at absolute zero. The temperature-dependent latent heat of vaporization of helium $L_{\mathrm{He}}(T)$ is an interpolation function, shown in Fig. S8 f), to the data extracted from (*73*). The equations 14,15,16 all together enable us to derive a temperature-dependent expression for the thermal resistance via evaporation $R_{\mathrm{vap}}(T) = (G_{\mathrm{vap}}(T))^{-1}$.

The temperature-dependent heat capacity of thin-film superfluid helium is given by $C_{\mathrm{He}}(T) = c_{\mathrm{He}}(T) m_{\mathrm{He}}$, with m_{He} being the superfluid helium mass covering the full microsphere (incl. stem) and $c_{\mathrm{He}}(T)$ an interpolation of the temperature-dependent specific heat for superfluid helium, with data obtained from (*73*) and shown in figure S8 d).

3.4 Transfer-function for the superfluid helium temperature $V_{\mathrm{He}}(\Omega, T)$

Having specified the electric analog of each thermal quantity in our system (see sections above) and simplified it to an electric circuit (see figure S7), enables us now to use simple electric calculation techniques to determine the bath-temperature dependent superfluid helium temperature $V_{\mathrm{He}}(\Omega, T)$ and its frequency response (transfer-function) to a fluctuating heat source. This gives us a full framework of our system so we can operate at the ideal temperature and frequency to maximise and control the fountain pressure backaction.

First we transform all thermal-electric quantities into the frequency domain, so they can

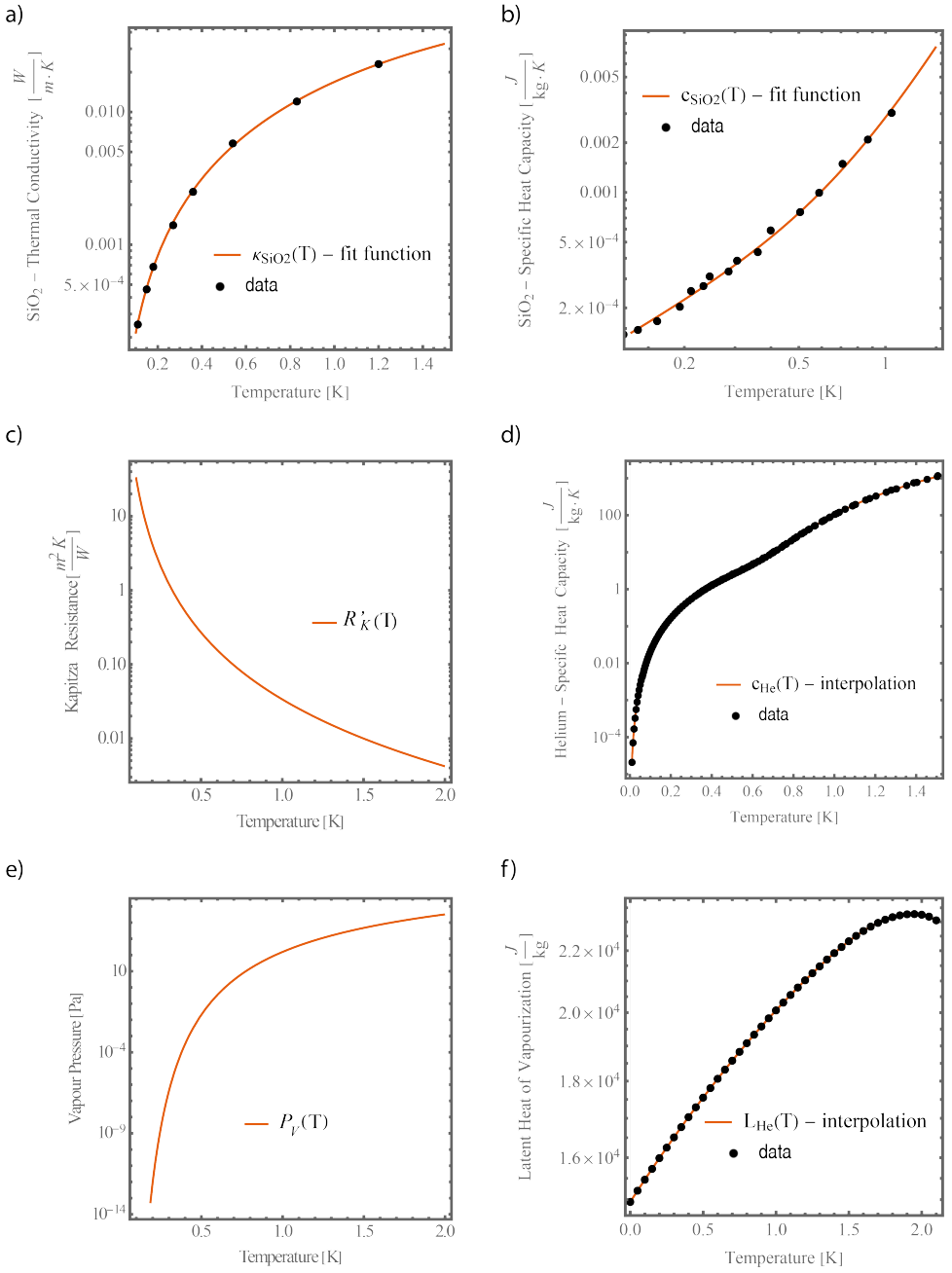

Figure S8: **Temperature-dependent material parameters.** Here we present all the temperature-dependent material parameters used for the thermal-electric analogy model. a) Fitted thermal conductivity $\kappa_{\mathrm{SiO_2}}(T)$ of silica with data points taken from literature (*79*). b) Fitted specific heat capacity $c_{\mathrm{SiO_2}}(T)$ with measured data from (*80*). c) Kapitza resistance of the interface between liquid He-II and silica (*81*). The figures d),e) and f) are all helium-related parameters. In d), we show the interpolated the specific heat capacity of helium $c_{\mathrm{He}}(T)$ obtained from the data in Ref. (*73*). e) plots the vapour pressure for helium, which is given in Ref. (*73*) in functional form (Eq. 16). In f) $L_{\mathrm{He}}(T)$ is the interpolation of the data for the latent heat of vaporization (*73*).

be written as complex impedances, which are all summarized in table S2. The total complex impedance for the substrate and superfluid helium are respectively given by:

$$\tilde{Z}_{\mathrm{sub}}(\Omega,T)=\left(\frac{1}{Z_{\mathrm{R_{sub}}}(T)}+\frac{1}{\tilde{Z}_{\mathrm{C_{sub}}}(\Omega,T)}\right)^{-1} \tag{17}$$

and

$$\tilde{Z}_{\mathrm{He}}(\Omega,T)=\left(\frac{1}{Z_{\mathrm{R_{vap}}}(T)}+\frac{1}{\tilde{Z}_{\mathrm{C_{He}}}(\Omega,T)}\right)^{-1}. \tag{18}$$

The combined impedance of superfluid helium and the Kapitza impedance is $\tilde{Z}_{\mathrm{KHe}}(\Omega,T)=\tilde{Z}_{\mathrm{He}}(\Omega,T)+Z_{\mathrm{K}}(T)$, as these two elements are in series, see Fig. S7. This leads to the total impedance of the circuit:

$$\tilde{Z}_{\mathrm{tot}}(\Omega,T)=\left(\frac{1}{\tilde{Z}_{\mathrm{sub}}(\Omega,T)}+\frac{1}{\tilde{Z}_{\mathrm{KHe}}(\Omega,T)}\right)^{-1}. \tag{19}$$

Therefore the voltage change (thermal realm: temperature) in the substrate is given by Ohm's law:

$$\tilde{V}_{\mathrm{sub}}(\Omega,T)=I_{\mathrm{ph}}\tilde{Z}_{\mathrm{tot}}(\Omega,T). \tag{20}$$

Considering the temperature drop over the Kapitza resistance, the temperature difference in the superfluid helium can be written as:

$$\begin{aligned}\tilde{V}_{\mathrm{He}}(\Omega,T)&=\tilde{V}_{\mathrm{sub}}(\Omega,T)-V_{\mathrm{K}}(T)\\&=I_{\mathrm{ph}}\tilde{Z}_{\mathrm{tot}}(\Omega,T)-\tilde{I}_{\mathrm{KHe}}(\Omega,T)Z_{\mathrm{K}}(T).\end{aligned} \tag{21}$$

The heat flow rate (electric-analogy: current) towards the superfluid helium $\tilde{I}_{\mathrm{KHe}}(\Omega,T)$ is given by Kirchhoff's law as:

$$\tilde{I}_{\mathrm{KHe}}(\Omega,T)=I_{\mathrm{ph}}-\tilde{I}_{\mathrm{sub}}(\Omega,T), \tag{22}$$

Using equations (20), (22) and the relation $\tilde{I}_{\mathrm{sub}}(\Omega,T)=\tilde{V}_{\mathrm{sub}}(\Omega,T)/\tilde{Z}_{\mathrm{sub}}(\Omega,T)$ in equation (21), results in:

$$\begin{aligned}\tilde{V}_{\mathrm{He}}(\Omega,T)&=I_{\mathrm{ph}}\tilde{Z}_{\mathrm{tot}}(\Omega,T)-\left(I_{\mathrm{ph}}-\frac{I_{\mathrm{ph}}\tilde{Z}_{\mathrm{tot}}(\Omega,T)}{\tilde{Z}_{\mathrm{sub}}(\Omega,T)}\right)Z_{\mathrm{K}}(T)\\&=I_{\mathrm{ph}}\left(\tilde{Z}_{\mathrm{tot}}(\Omega,T)-Z_{\mathrm{K}}(T)+\frac{Z_{\mathrm{K}}(T)\tilde{Z}_{\mathrm{tot}}(\Omega,T)}{\tilde{Z}_{\mathrm{sub}}(\Omega,T)}\right).\end{aligned} \tag{23}$$

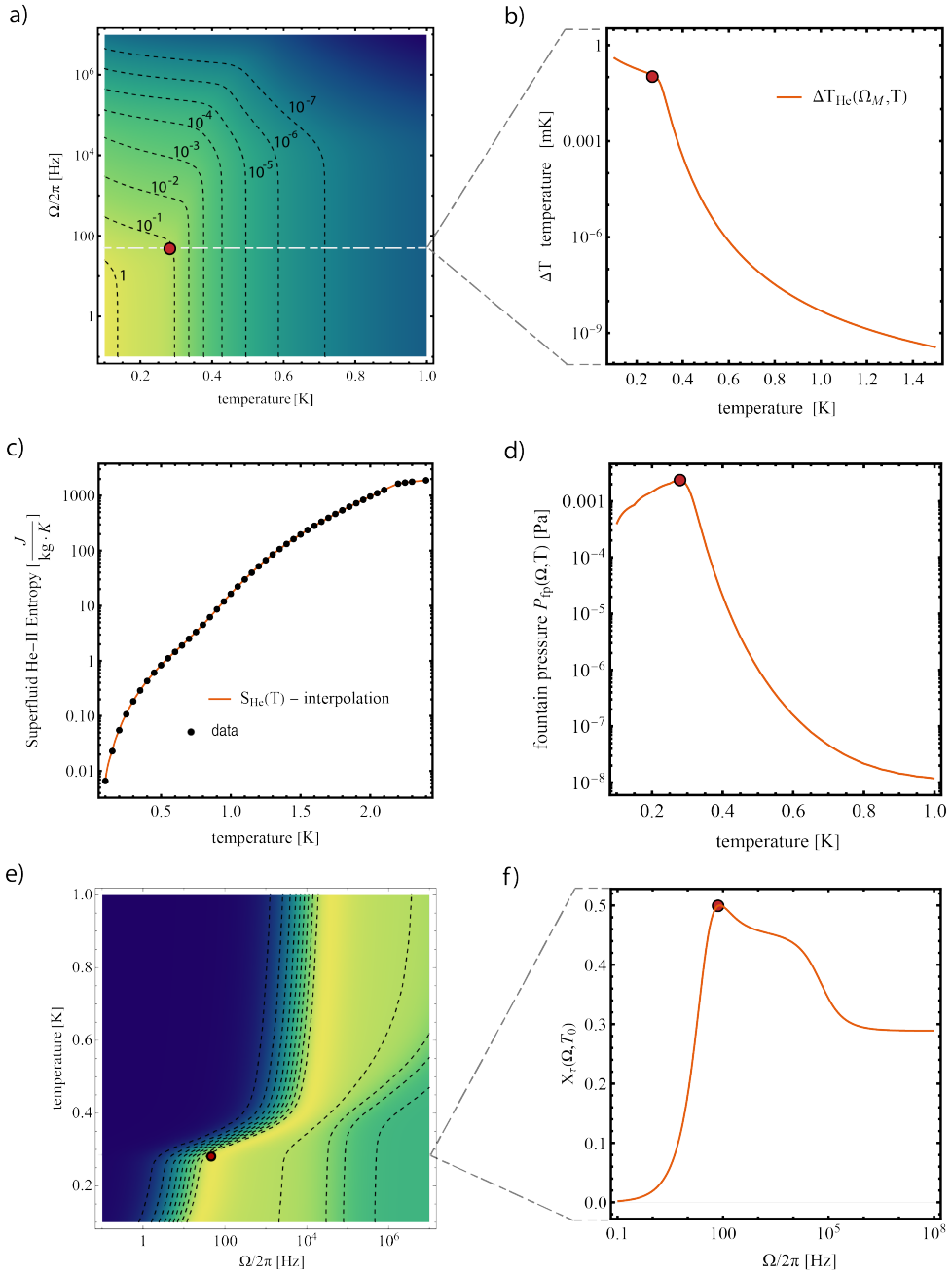

Figure S9: **Modelled transfer functions of the experimental system.** In all figures the red dot represents the operation point of the experimental system. Figure a) shows a contour-color plot of the superfluid helium temperature increase $\Delta T_{\mathrm{He}}(\Omega, T)$ and its dependency on the thermal bath temperature T and the modulation frequency Ω. b) is a line plot of $\Delta T_{\mathrm{He}}(\Omega_{\mathrm{M}}, T)$ at the experimental mechanical frequency Ω_{M}. Figure c) shows the interpolation function $S_{\mathrm{He}}(T)$ along with the data of entropy of superfluid helium from (*73*). d) plots the superfluid helium fountain pressure $P_{\mathrm{fp}}(\Omega_M, T)$. e) is a contour-color plot of the dynamical backaction function $\chi_{\mathrm{He}}(\Omega, T)$ and f) is a 2D plot of the same function at the given bath temperature $T = 284\,\mathrm{mK}$.

The voltage here is a complex number. The real temperature increase in the superfluid helium film and the substrate are given by the modulus of the voltage:

$$\Delta T_{\mathrm{He}}(\Omega, T) = V_{\mathrm{He}}(\Omega, T) = |\tilde{V}_{\mathrm{He}}(\Omega, T)| \tag{24}$$

and

$$\Delta T_{\mathrm{sub}}(\Omega, T) = V_{\mathrm{sub}}(\Omega, T) = |\tilde{V}_{\mathrm{sub}}(\Omega, T)|. \tag{25}$$

Fig. S9 (a) and (b) demonstrate $\Delta T_{\mathrm{He}}(\Omega, T)$ and its dependency on the bath temperature T and the drive frequency Ω for an absorbed power of $I_{\mathrm{ph}} = 1\,\mathrm{pW}$, where the red dot displays the operation point of our experimental system. Together with the temperature dependent entropy $S_{\mathrm{He}}(T)$, which is given by an interpolation to some measured data from (*73*) (see figure S9 c)), the fountain pressure takes the form:

$$P_{\mathrm{fp}}(\Omega, T) = \rho_{\mathrm{He}}\, S_{\mathrm{He}}(T)\, \Delta T_{\mathrm{He}}(\Omega, T), \tag{26}$$

and is plotted in figure S9 d) for the experimental mechanical frequency Ω_{M}. This model shows that our operation temperature of $T = 284\,\mathrm{mK}$ is the optimal temperature that results in the maximum fountain pressure for our system. This maximum arises as a consequence of two competing trends. On one hand, the entropy is an increasing function of T, pointing towards a stronger fountain pressure interaction at higher temperatures (Fig.S9c). On the other hand, the increase in heat capacity and thermal conductivity at higher temperatures reduces the temperature rise ΔT, counteracting the previous effect (Fig.S9b). The fountain pressure force is finally:

$$F_{\mathrm{fp}}(\Omega, T) = P_{\mathrm{fp}}(\Omega, T)\mathcal{A}, \tag{27}$$

with $\mathcal{A}$ being the surface area of the whole resonator.

3.5 Thermal response time

In addition to maximising $\Delta T_{\rm He}(\Omega, T)$ to optimise the fountain pressure strength, it is also important to understand and optimize the dynamical backaction efficiency of the system. The theory of photothermal heating and cooling (*17, 20*) shows that strongest backaction is achieved in the regime $\Omega_{\rm M}\,\tau_{\rm th} \sim 1$, where $\tau_{\rm th}$ corresponds to the thermal response time of the superfluid film. The thermal time delay $\tau_{\rm th}$ is given by the relation $\tau_{\rm th} = \phi/\Omega$, with Ω the mechanical frequency and ϕ the phase of the complex transfer function $\tilde{V}_{\rm He}(\Omega, T)$:

$$\phi_{\rm He}(\Omega, T) = \arg(\tilde{V}_{\rm He}(\Omega, T)), \tag{28}$$

which means that $\tau_{\rm th}$ is frequency- and temperature-dependent. The unitless functional form:

$$\chi_{\rm He}(\Omega, T) = \frac{\Omega\tau_{\rm th}((\Omega, T))}{1 + (\Omega\tau_{\rm th}((\Omega, T)))^2}, \tag{29}$$

represents the optimal time delay of the bolometric forces (*16–19*). For $\Omega_{\rm M}\,\tau_{\rm th} \sim 1$ we get $\chi_{\rm He}(\Omega = 1/\tau_{\rm th}, T) = 0.5$. Fig. S9(e) shows $\chi_{\rm He}(\Omega, T)$ in a color-contour plot for our system. Fig. S9(f) is a line cut through (e) for a fixed temperature of 284 mK. The red dot marks the mechanical mode frequency $\Omega_{\rm M}$ of the system, which is at the maximum value of 0.5 for $\chi_{\rm He}$. As a consequence, our choice of superfluid mechanical mode and cryostat temperature allows us to operate at both the optimal point for fountain pressure strength (Fig.S9d), and optimal time-delayed forcing for dynamical backaction (Fig.S9f).

3.6 Figure of merit - fountain pressure dynamical backaction optimization

The two main dynamical forces in our system are the fountain pressure force and the radiation pressure force given by:

$$F_{\rm rad} = n_{\rm cav}\hbar G, \tag{30}$$

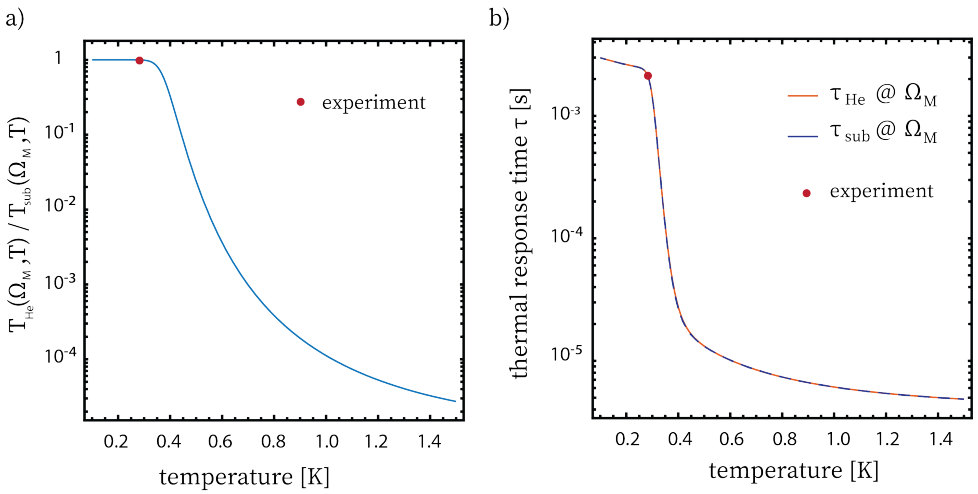

Figure S10: **Temperature ratio and thermal response time of superfluid helium and the substrate**. At the frequency and temperature used in the experiments (red dot), the temperature of the film closely tracks that of the underlying silica resonator, allowing these to be modelled as a common element in the ODE simulations of section 4.

where n_{cav} is the intracavity photon number, $\hbar$ the reduced Planck constant and G the optomechanical coupling rate. Having the two forces, fountain pressure force and radiation pressure force, and the dynamical backaction efficiency $\chi_{\mathrm{He}}(\Omega, T)$ leads to a figure of merit for the photothermal effect in our system:

$$f_{\mathrm{M}}(\Omega, T) = \frac{F_{\mathrm{fp}}(\Omega, T)}{F_{\mathrm{rad}}} \chi_{\mathrm{He}}(\Omega, T). \tag{31}$$

4 Numerical model

Differential equations

The dynamical behaviour of the superfluid resonator may be described by three coupled differential equations relating to the intracavity photon number n_{cav}, the change in mean film thickness at the level of the WGM x and the temperature T. Each of these parameters respectively responds on a characteristic timescale of $1/\kappa \sim$ ns; $\tau_{\mathrm{th}} \sim$ ms and $1/\Gamma \sim$ s. Since the optical decay rate κ is much larger than all other decay rates, we consider that the intracavity

photon number n_{cav} reacts instantaneously to any changes in the cavity (adiabatic limit), such that it takes the steady-state form (*11*):

$$|a|^2 = n_{\mathrm{cav}} = \frac{\kappa_{\mathrm{ex}}}{\Delta^2 + \left(\frac{\kappa}{2}\right)^2} \frac{P}{\hbar \omega_L}, \tag{32}$$

where $\kappa = \kappa_{\mathrm{ex}} + \kappa_i$ is the sum of the extrinsic and intrinsic loss rates respectively (*11*), and P the laser power at the level of the fiber taper. The detuning Δ is equal to:

$$\Delta = \Delta_0 + Gx \quad \text{with} \quad G = \frac{\partial \omega_0}{\partial x}, \tag{33}$$

with Δ_0 the cavity detuning for zero displacement and G the optomechanical coupling rate (see section 2.5). The dynamics can thus be reduced to two coupled equations of motion. The first determines the motion of the superfluid film:

$$m_{\mathrm{eff}}\, \ddot{x} + m_{\mathrm{eff}}\, \Gamma\, \dot{x} + m_{\mathrm{eff}}\, \Omega^2\, x = F_{\mathrm{fp}} = \rho\, S(T_0)\, (T - T_0)\, \mathcal{A}, \tag{34}$$

where T_0 and T are respectively the temperature of the environment and that of the superfluid film covering the resonator. This equation, which assumes a constant value for the entropy $S(T_0)$ is valid in the limit $\Delta T \ll T_0$, which is the case in the experiments. The second governs the evolution of the temperature T and arises from conservation of energy:

$$\dot{T} = \frac{n_{\mathrm{cav}}\, \hbar\, \omega_L\, \kappa_i\, \alpha_{\mathrm{abs}}}{m\, c} - \frac{G_{\mathrm{th}}(T_0)\, (T - T_0)}{m\, c} \tag{35}$$

Here, $\alpha_{\mathrm{abs}} \in [0, 1]$ corresponds to the fraction of the intrinsic losses dissipated as heat in the resonator, m to the resonator's thermal mass and c its specific heat capacity, and $G_{\mathrm{th}} = \frac{m\, c}{\tau_{\mathrm{th}}}$ the resonator's thermal conductance. We note here that at the operational point used in the experiments ($\Omega/2\pi = 72$ Hz; $T = 284$ mK) and the low optical powers in the pW range, the superfluid film temperature closely tracks that of the silica microsphere with minimal temperature difference and phase lag (verified through the thermal model of section 3, and plotted in Fig. S10). For this reason, in these time-domain numerical simulations, we simplify the thermal

system by considering the silica resonator and superfluid film as a common element, of mass m and heat capacity c, dominated by the microsphere mass and heat capacity. This allows us to accurately reproduce the experimental results, as shown below. The time dynamics of our system are obtained by numerically solving the coupled differential equations (Eqs (34) and (35)) with an ODE solver (MATLAB software).

Numerical simulations results

Solving these equations with the parameters provided in Table S3, we obtain the dynamical behaviour of the superfluid film displacement $\Delta x(t)$, normalized optical output power $|a_{\mathrm{out}}(t)|^2/|a_{\mathrm{in}}|^2$ (where $|a_{\mathrm{out}}(t)|^2$ and $|a_{\mathrm{in}}(t)|^2$ are respectively the output and input optical powers, and are related via input-output formalism (*11, 83*)) and the temperature fluctuations $\Delta T(t)$ around the environment temperature of $T = 284\,\mathrm{mK}$. The sub-figures c), d) and e) in figures S11, S12 and S13 show the time-dependency of these parameters in the steady-state phonon lasing regime (i.e. after the initial transient dynamics) at the input powers 3.4 pW, 6.8 pW and 68 pW. The simulations are performed at a cavity detuning where the superfluid film's motional amplitude is maximized (represented by the red dot in sub-figure a)). To appropriately compare the numerical simulations with the measurements, done with a spectrum analyzer and with a heterodyne detection scheme, we added an optical local oscillator field and applied a Fourier transformation to the time-dependent normalized optical output field in the steady state regime of the system for different cavity detunings and optical input powers. The black line in all sub-figures a) of figures S11, S12 and S13 demonstrates the peak value of the fundamental mechanical mode in the normalized spectral density versus cavity detuning for different input powers. This we compared to the normalized amplitudes of the measured mechanical mode at different cavity detunings as well and same input powers, which are displayed as blue dots in all sub-figures a) of figures S11, S12 and S13. The numerical simulation is fitted to the experi-

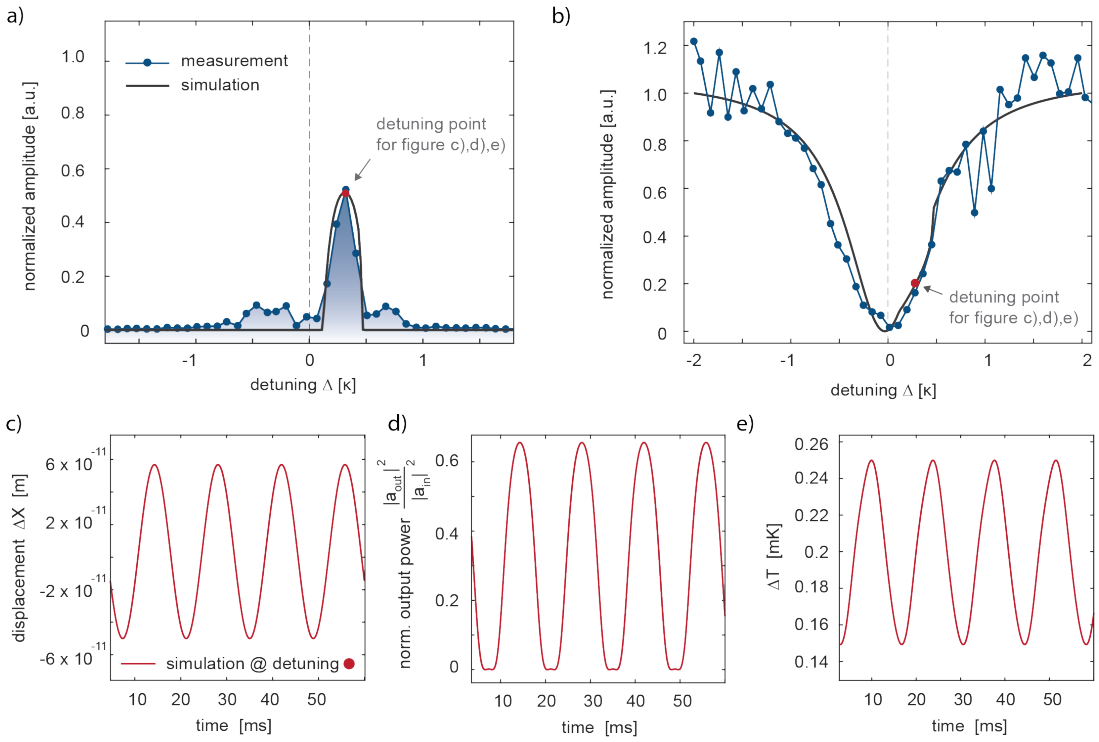

Figure S11: **Numerical simulation for 3.4 pW input power.** a) Mechanical mode ($\Omega/2\pi = 72$ Hz) amplitude as a function of cavity detuning, where the blue dots represent the normalized measured mode peak of the power spectrum and the black line the numerical simulations. b) Normalized optical transmission of the whispering gallery mode resonator depending on the detuning, obtained by plotting the experimentally measured normalized spectral density peak value of the calibration peak at 180 Hz (blue dots) and the local oscillators (80 MHz) normalized spectral density peak value in the numerical simulations (black line). The numerical simulations in c), d) and e) show the time dependency in the steady state regime of respectively the displacement ΔX, the cavity transmitted normalized optical power and the temperature fluctuation ΔT around $T_0 = 284$ mK. These simulations are performed at the detuning represented by the red dot in a) and b).

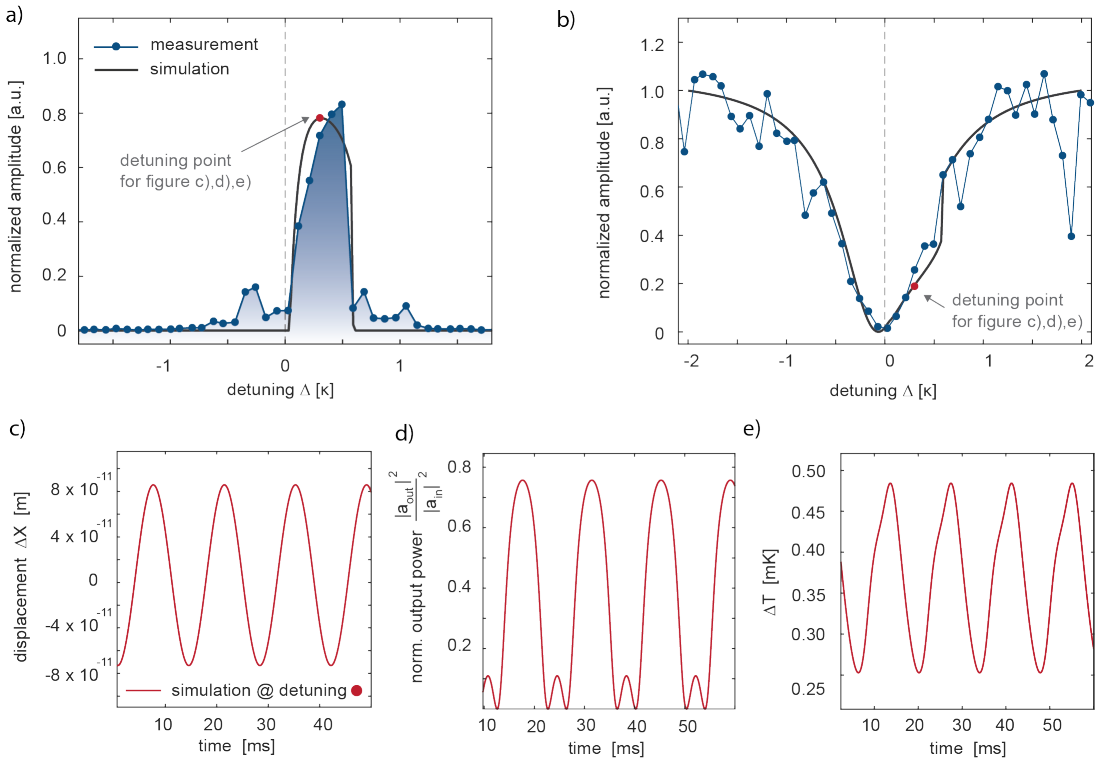

Figure S12: **Numerical simulation for 6.8 pW input power.** a) Mechanical mode ($\Omega/2\pi = 72$ Hz) amplitude as a function of cavity detuning, where the blue dots represent the normalized measured mode peak of the power spectrum and the black line the numerical simulations. b) Transmitted optical power from of the whispering gallery mode depending on the detuning, obtained by plotting the experimentally measured normalized spectral density peak value of the calibration peak at 180 Hz (blue dots) and the local oscillators (80 MHz) normalized spectral density peak value in the numerical simulations (black line). The numerical simulations in c), d) and e) show the time dependency in the steady-state regime of respectively the displacement ΔX, the cavity transmitted normalized optical power and the temperature fluctuation ΔT around $T_0 = 284$ mK. These simulations are performed at the detuning represented by the red dot in a) and b).

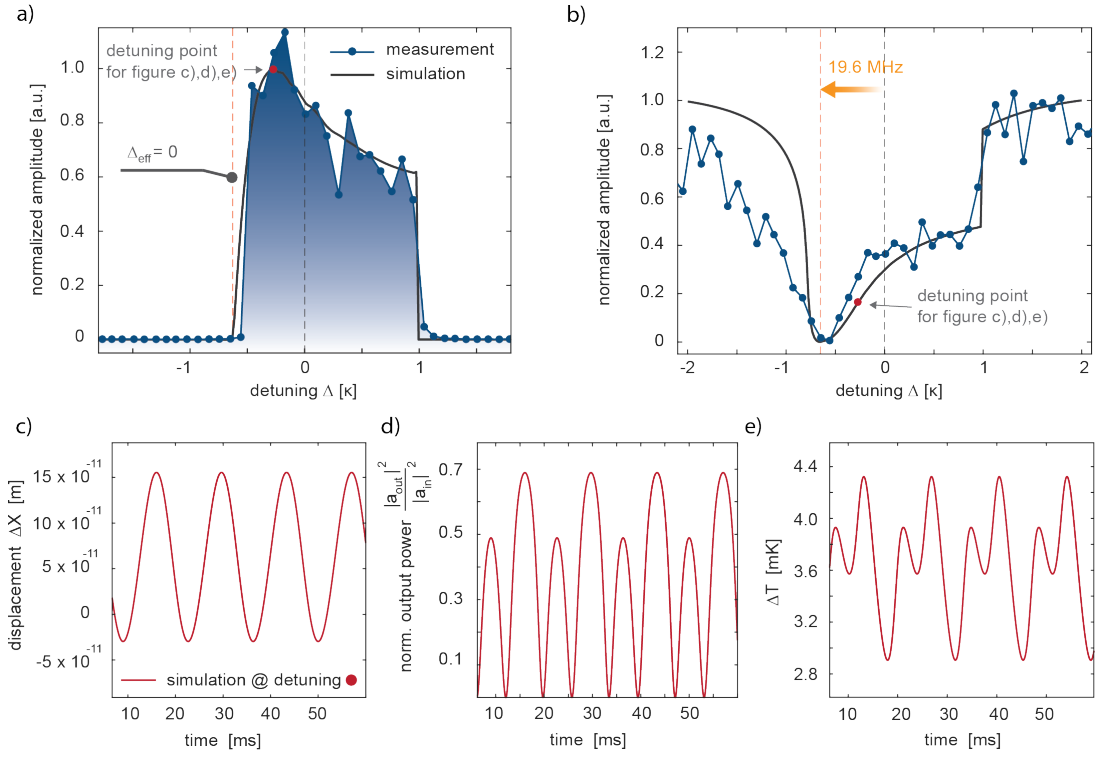

Figure S13: **Numerical simulation for 68 pW input power.** a) shows the mechanical mode ($\Omega/2\pi = 72$ Hz) amplitude depending on the cavity detuning, where the blue dots represent the normalized measured mode peak of the power spectrum and the black line the numerical simulations. b) Normalized optical transmission of the whispering gallery mode resonator as a function of detuning, obtained by plotting the experimentally measured normalized spectral density peak value of the calibration peak at 180 Hz (blue dots) and the local oscillators (80 MHz) normalized spectral density peak value in the numerical simulations (black line). At this high power, the D fountain pressure force causes the superfluid film to thicken, which leads to an optical resonance shift of 19.6 MHz. The numerical simulations in c), d) and e) show the time dependency in the steady state regime of respectively the displacement Δx, the cavity transmitted normalized optical power and the temperature fluctuation ΔT around $T_0 = 284$ mK. These simulations are performed at the detuning represented by the red dot in a) and b).

mental data by using α_{abs}, the fraction of dissipated optical power that gets converted into heat in the resonator, and the mechanical mode decay rate Γ as fitting parameters. The best results could be obtained with $\alpha_{\mathrm{abs}} = 0.35$ and Γ being 1 Hz, 1.5 Hz and 5 Hz respectively for the input powers 3.4 pW, 6.8 pW and 68 pW, pointing towards an increase in the intrinsic damping rate with laser power. Such nonlinear damping has already been reported in the context of superfluid helium films (*84*), as well as silicon optomechanical crystals (*22*). In addition to the strong dynamical back action, induced by the photo thermal effect, we observe a static photothermal effect in the simulations as well. As explained in the main text, this static effect is caused by the rise of the mean temperature of the superfluid film. In sub-figure e) of the figures S11, S12 and S13 it is shown that the mean temperature rises by about 0.2 mK, 0.37 mK and 3.6 mK respectively for the input powers 3.4 pW, 6.8 pW and 68 pW. This increase in temperature causes the superfluid film to thicken, shifting the optical mode. For the input power of 68 pW the optical mode is shifted by 19.6 MHz, corresponding to an optical tunability of 288 GHz/μW, as shown in Fig. S13(b). This DC thicknening of the film is also apparent in Fig. S13(c), which shows the superfluid film oscillations around a new, thicker equilibrium position.

We note that the simplified equation solved for the mechanical oscillator Eq. (34) only includes a viscous damping term and a driving force through the fountain pressure interaction. It does not include a thermal Langevin force, and as such the only steady-state endpoints of the simulation correspond to a large motional amplitude if the optomechanical gain exceeds the intrinsic losses of the resonator, or zero motional amplitude if the optomechanical gain is less than the resonator losses, as is the case for a red-detuned laser beam (*11*). In contrast, the collected experimental data is sensitive to the thermal Brownian motion of the oscillator, accounting for the discrepancy between simulation and experimental data visible for negative (i.e. red) detuning in Fig. S11(a) and Fig. S12(a). This discrepancy becomes proportionally smaller at higher optical powers (Fig. S13(a)).

Parameter	Symbol	Value	Unit	Source
WGM intrinsic energy decay rate	$\kappa_i/2\pi$	15	MHz	measurement
WGM extrinsic energy decay rate	$\kappa_{\rm ex}/2\pi$	15	MHz	measurement
Third sound mode frequency	$\Omega_M/2\pi$	72	Hz	measurement
		86	Hz	FEM
Third sound mode effective mass	$m_{\rm eff}$	5.1×10^{-3}	kg	FEM
Third sound mode decay rate	Γ	$2\pi \times 1$	Hz	measurement
Optomechanical coupling strength	$G/2\pi$	0.2 ± 0.01	GHz/nm	FEM
Single photon optomechanical coupling rate	$g_0/2\pi$	0.7	Hz	FEM
Microsphere radius	R	49.5	μm	SEM
Mean superfluid film thickness	d_0	24	nm	measurement
Superfluid ^{4}He density	$\rho_{\rm He}$	145	kg/m^3	(*73*)
First sound speed in superfluid helium	$c_{1_{\rm He}}$	236	m/s	(*85*)
superfluid helium mass (covering the total microsphere+stem)	$m_{\rm He}$	2.65×10^{-12}	kg	FEM
Silica density	$\rho_{\rm SiO_2}$	2200	kg/m^3	(*86*)
Silica thermal conductivity (@284 mK)	$\kappa_{\rm SiO_2}$	1.6×10^{-3}	W/m/K	(*87*)
Silica specific heat capacity (@284 mK)	$c_{\rm SiO_2}$	3.4×10^{-4}	J kg^{-1} K^{-1}	(*34*)
Thermal conductance (@284mK)	$G_{\rm th-sub}$	4.1×10^{-9}	W/K	FEM
Silica microsphere area (incl. stem)	$\mathcal{A}$	7.7×10^{-7}	m^2	SEM
Silica microsphere mass (incl. stem)	$m_{\rm sub}$	4.9×10^{-8}	kg	FEM
Longitudinal sound velocity of silica	$c_{l_{\rm SiO_2}}$	5968	m/s	(*88*)
Transverse sound velocity of silica	$c_{t_{\rm SiO_2}}$	3764	m/s	(*88*)
Thermal response time	$\tau_{\rm th}$	5.7	ms	FEM
He II entropy per unit mass (@284 mK)	S	0.16	J/kg/K	(*73*)
fraction of κ_i dissipated as heat	$\alpha_{\rm abs}$	0.35	-	fit
Operating temperature	T	284	mK	measurement

Table S3: **Physical parameters used in the simulation.** FEM:Finite Element modelling. SEM: Scanning electron microscope.

5 Lasing thresholds for various systems

We benchmark our phonon lasing threshold against existing literature in Fig. 5 of the main text and Fig. S14. We condensed the amount of systems shown in Fig. 5 and Fig. S14 to 18 different experiments, which are representative for the majority of phonon lasing systems and driving mechanisms (radiation pressure, electrostriction, photothermal and electrothermal interactions). All literature references that have been used for Fig. 5 are listed in Table S4. We additionally plot the phonon lasing thresholds of these same experiments versus resonator spring constant and resonator mass in Fig. S14. We choose to focus our benchmark on the threshold power P_{thresh}, i.e., the incident optical power, (and not on the intracavity photon number at threshold $n_{\mathrm{cav\,thresh}}$) as this is the value which is most widely reported in the literature. The conversion between the two is given by (*11*):

$$n_{\mathrm{cav\,thresh}} = \frac{\kappa_{\mathrm{ex}}}{\Delta^2 + (\kappa/2)^2} \frac{P_{\mathrm{thresh}}}{\hbar\,\omega}, \tag{36}$$

where κ_{ex} and Δ are respectively the extrinsic coupling rate of the cavity and the laser-cavity detuning and $\kappa = \kappa_0 + \kappa_{\mathrm{ex}}$ is the total cavity loss rate, corresponding to the sum of intrinsic and extrinsic loss rates. Systems in the good-cavity limit ($\Omega \gg \kappa$) can achieve phonon lasing at comparatively lower intracavity photon number (*22*), as the optical to mechanical energy conversion efficiency *per intracavity photon* is high. However the overall efficiency *per launched laser photon* is limited by the lower rate at which photons enter the cavity in the good cavity limit, when the laser is highly detuned from the cavity resonance (*11*).

6 Thermodynamic efficiency

The thermodynamic efficiency is estimated by multiplying the stored mechanical power with the mechanical damping rate, yielding an acoustic power loss P_{mech}, which must be exactly

Ref. #	mechanical frequency	effective mass	lasing threshold	driving mechanism	Source
(*24*)	90 MHz	2.7×10^{-21} kg	~ 5 pW	electrothermal	C. Urgell, W. Yang, S. L. De Bonis, C. Samanta, M. J. Esplandiu, Q. Dong, Y. Jin, and A. Bachtold, Cooling and Self-Oscillation in a Nanotube Electromechanical Resonator, *Nature Physics* vol.**16**, pp.32–37 (2020)
(*23*)	230 MHz	2.2×10^{-20} kg	~ 10 pW	electrothermal	Y. Wen, N. Ares, F. J. Schupp, T. Pei, G. a. D. Briggs, and E. A. Laird, A Coherent Nanomechanical Oscillator Driven by Single-Electron Tunnelling,*Nature Physics* vol.**16**, pp.75–82 (2020)
(*89*)	3.5 MHz	2×10^{-16} kg	500 nW	photothermal	R.A. Barton, et al, Photothermal Self-Oscillation and Laser Cooling of Graphene Optomechanical Systems, *Nano Letters* vol.**12**, **9**, pp. 4681–4686 (2012)
(*90*)	3 MHz	2.1×10^{-16} kg	660 nW	photothermal	R. De Alba, T. S. Abhilash, R. H. Rand, H. G. Craighead, and J. M. Parpia, Low-Power Photothermal Self-Oscillation of Bimetallic Nanowires, *Nano Letters* vol.**17**, **7**, pp.3995–4002 (2017)
(*91*)	180 kHz	1.6×10^{-12} kg	30 μW	photothermal	D. Woolf, P.-C. Hui, E. Iwase, M. Khan, A. W. Rodriguez, P. Deotare, I. Bulu, S. G. Johnson, F. Capasso, and M. Loncar, Optomechanical and Photothermal Interactions in Suspended Photonic Crystal Membranes, *Optics Express* vol.**21**, **6**, pp. 7258-7275 (2013)
(*20*)	8 kHz	2.3×10^{-12} kg	26 μW	photothermal	C. Metzger, M. Ludwig, C. Neuenhahn, A. Ortlieb, I. Favero, K. Karrai, and F. Marquardt, Self-Induced Oscillations in an Optomechanical System Driven by Bolometric Backaction, *Physical Review Letters* vol.**101**, 133903 (2008)
(*29*)	7.3 MHz	$m_{\rm eff} \sim 10^{-14}$ kg $m_{\rm film} \sim 10^{-16}$ kg	1.8 μW	photothermal/radiation pressure	X. He, G. I. Harris, C. G. Baker, A. Sawadsky, Y. L. Sfendla, Y. P. Sachkou, S. Forstner, and W. P. Bowen, Strong Optical Coupling through Superfluid Brillouin Lasing, *Nature Physics* vol.**16**, pp.417–421 (2020)
(*92*)	314 MHz	5.3×10^{-14} kg	$\sim$50 μW	photothermal/radiation pressure	P. E. Allain, B. Guha, C. Baker, D. Parrain, A. Lemaître, G. Leo, and I. Favero, Electro-Optomechanical Modulation Instability in a Semiconductor Resonator, *Physical Review Letters* vol.**126**, 243901 (2021)
(*93*)	3 GHz	2.7×10^{-16} kg	2.5 mW	radiation pressure	L. Mercadé, L. L. Martín, A. Griol, D. Navarro-Urrios, and A. Martínez, Microwave Oscillator and Frequency Comb in a Silicon Optomechanical Cavity with a Full Phononic Bandgap, *Nanophotonics* vol.**9**(11), pp.3535–3544 (2020)
(*94*)	3 GHz	1.0×10^{-15} kg	40 μW	photoelastic	I. Ghorbel et al., Optomechanical Gigahertz Oscillator Made of a Two Photon Absorption Free Piezoelectric III/V Semiconductor, *APL Photonics* vol.**4**, pp.116103 (2019)
(*95*)	2 MHz	7.6×10^{-15} kg	60 μW	radiation pressure	H. Jayakumar, B. Khanaliloo, D. P. Lake, and P. E. Barclay, Tunable Amplification and Cooling of a Diamond Resonator with a Microscope, *Phys. Rev. Applied* vol.**16**, 014063 (2021)
(*96*)	23 MHz	5.0×10^{-11} kg	7 μW	radiation pressure	I. S. Grudinin, H. Lee, O. Painter, and K. J. Vahala, Phonon Laser Action in a Tunable Two-Level System, *Physical Review Letters* vol.**104**, 083901 (2010)
(*97*)	1.2 GHz	5.7×10^{-15} kg	3 μW	radiation pressure	W. C. Jiang, X. Lu, J. Zhang, and Q. Lin, High-Frequency Silicon Optomechanical Oscillator with an Ultralow Threshold, *Optics Express* vol.**20**,14, pp. 15991-15996 (2012)
(*98*)	8 MHz	1.5×10^{-13} kg	270 nW	radiation pressure	Q. Lin, J. Rosenberg, X. Jiang, K. Vahala, and O. Painter, Mechanical Oscillation and Cooling Actuated by the Optical Gradient Force, *Physical Review Letters* vol.**103**, 103601 (2009)
(*42*)	3.7 GHZ	3.1×10^{-16} kg	$\sim$ 500 nW	radiation pressure/ electrostriction	A. G. Krause, J. T. Hill, M. Ludwig, A. H. Safavi-Naeini, J. Chan, F. Marquardt, and O. Painter, Nonlinear Radiation Pressure Dynamics in an Optomechanical Crystal, *Physical Review Letters* vol.**115**, 233601 (2015)
(*22*)	3.6 GHz	$\sim 3 \times 10^{-16}$ kg	7 nW	radiation pressure/ electrostriction	S. M. Meenehan, J. D. Cohen, S. Gröblacher, J. T. Hill, A. H. Safavi-Naeini, M. Aspelmeyer, and O. Painter, Silicon Optomechanical Crystal Resonator at Millikelvin Temperatures, *Phys. Rev. A* vol.**90**, 011803 (2014)
(*32*)	1.35 MHz	$\sim 3 \times 10^{-11}$ kg	50 μW	photothermal/radiation pressure	D. L. McAuslan, G. I. Harris, C. Baker, Y. Sachkou, X. He, E. Sheridan, and W. P. Bowen, Microphotonic Forces from Superfluid Flow, *Physical Review X* vol.**6**, 021012 (2016)
(*27*)	482 kHz	$m_{\rm eff} \sim 10^{-11}$ kg $m_{\rm film} \sim 10^{-15}$ kg	200 nW	photothermal/radiation pressure	G. I. Harris, D. L. McAuslan, E. Sheridan, Y. Sachkou, C. Baker, and W. P. Bowen, Laser Cooling and Control of Excitations in Superfluid Helium, *Nature Physics* vol.**12**, 788–793 (2016)

Table S4: **Sources used to compare the lasing thresholds for various systems in Fig.5.**

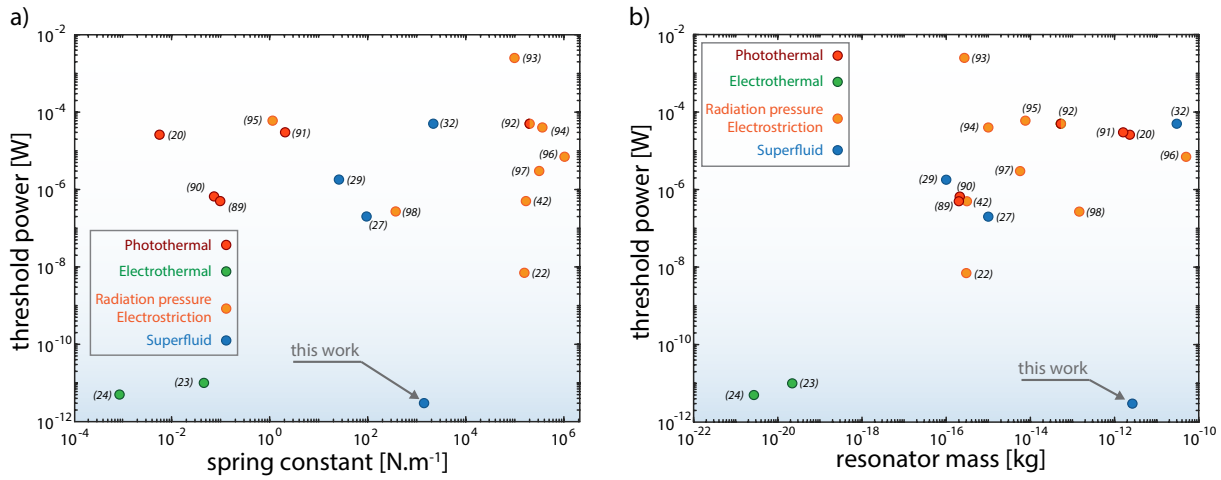

Figure S14: **Phonon lasing thresholds of different optomechanical and electromechanical experiments.** These are plotted versus (a) resonator spring constant and (b) resonator mass. Details on the reference publication for each point can be found in Table S4. While Ref. (*32*) considered the vibrational mode of silica microtoroid, we have classified it under 'Superfluid' as the superfluid helium film coating the device provided enhanced dynamical backaction.

compensated by the optical drive to maintain constant amplitude self-sustained oscillations.

$$P_{\rm mech} = \frac{1}{2} m_{\rm eff} \Omega^2 x^2 \Gamma \tag{37}$$

Using the values from Table S3 and a displacement amplitude of $x = 6 \times 10^{-11}$ (obtained from Fig. S11), we get $P_{\rm mech} = 1.2 \times 10^{-17}$ W; while the dissipated optical power is given by $P_{\rm abs} = P \times \alpha_{\rm abs} = 3.4\,{\rm pW} \times 0.35 = 1.2\,{\rm pW}$. This results in a thermodynamic efficiency (rate of conversion of heat into mechanical work) of $\eta = P_{\rm mech}/P_{\rm abs} = 1 \times 10^{-5}$.

As a comparison we calculate the thermodynamic efficiency for the carbon nanotube electrothermal system with the closest lasing threshold ($\sim$ 5 pW) (*24*). The mechanical power produced to sustain phonon-lasing is:

$$P_{\rm mech}^{\rm nano} = \frac{1}{2} m_{\rm eff}^{\rm nano} \Omega_{\rm nano}^2 x_{\rm nano}^2 \Gamma_{\rm nano} = 4.3 \times 10^{-19}\,{\rm W}, \tag{38}$$

with the effective mass $m_{\rm eff}^{\rm nano} = 2.7 \times 10^{-21}$ kg, the mechanical frequency $\Omega_{\rm nano}/(2\pi) = 90$ MHz, the displacement $x_{\rm nano} = 4$ nm and the mechanical decay rate $\Gamma_{\rm nano}/(2\pi) = 10$ Hz (*24*).

The electrical power dissipated as heat required for the production of $P_{\mathrm{mech}}^{\mathrm{nano}}$ is approximately $P_{\mathrm{elec}} = 5\,\mathrm{pW}$. This results in an thermodynamic efficiency for the nanotubes $\eta_{\mathrm{nano}} = P_{\mathrm{mech}}^{\mathrm{nano}}/P_{\mathrm{elec}} = 0.86 \times 10^{-7}$. This comparison indicates our system is $\sim 10^2$ times more thermodynamically efficient than the nanotube system with the lowest reported lasing threshold, aside from ours.

7 High-amplitude wave regime

Our work provides for the first time the combination of high precision optomechanical read-out—capable of measuring superfluid waves with sub-monolayer thickness precision and micrometer spatial resolution—with an actuation capability sufficiently strong to reach the highly nonlinear regime where the wave amplitude becomes comparable to the film thickness. This is a prerequisite to study the nonlinear fluid dynamics of superfluid helium films, which has been a longstanding goal in the field (*99*). An example of the measured power spectral density in this regime is shown in Fig. S15. It is measured with nanowatts of incident power and a superfluid film thickness $d \simeq 8$ nm, at which lasing occurs preferentially on the third order stem mode, as shown in Fig. S15 right. More than a hundred higher order harmonics are visible in this high-amplitude regime, in which we estimate $\eta \sim d$ through the time-domain optical output of the cavity.

8 Single photon detection

The fountain pressure between a region of the film at temperature T, and a bath at temperature T_0 corresponds to

$$P_{\mathrm{fp}} = \rho \int_{T_0}^{T} S(T')\,\mathrm{d}T' \tag{39}$$

For a small difference in temperature, the fountain pressure is given by (*33, 34*):

$$P_{\mathrm{fp}} = \rho S\,\Delta T \tag{40}$$

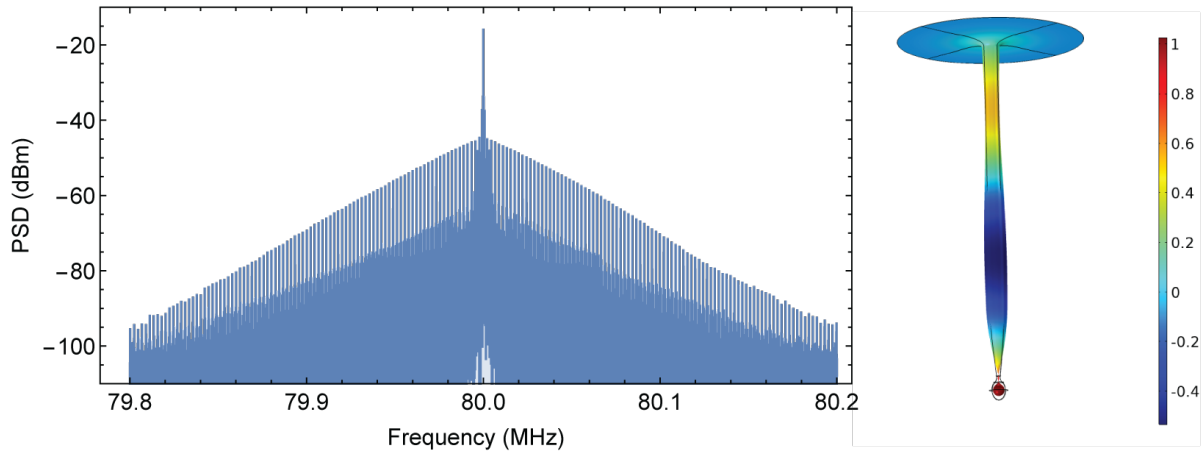

Figure S15: **High-amplitude wave regime.** Left: Optical readout of the superfluid's acoustic motion performed with a heterodyne detection scheme with a local oscillator field offset by 80 MHz (see Figure 3 of the main text). Right: Finite element modelling of the third-order stem mode, oscillating at 2.2 kHz. Color represents the superfluid displacement amplitude, normalized such that $\max(\eta) = 1$.

At low temperatures, the specific heat of superfluid helium is several orders of magnitude larger than that of the underlying optical resonator material (e.g. silicon, silica) (*100*). For instance, at 250 mK, $c_{\mathrm{He}} \simeq 1000\, c_{\mathrm{SiO2}}$. Therefore for miniature optical resonators, where the thickness of the superfluid film is no longer negligible compared to that of the resonator (consider e.g. a 30 nm thick superfluid film on either side of a 200 nm thick resonator), the entire thermal mass of the superfluid-covered resonator is dominated by the superfluid film. The temperature increase for a deposited energy Q corresponding to one absorbed photon is therefore given by:

$$\Delta T = \frac{Q}{m\, c_{\mathrm{He}}} = \frac{\hbar\omega}{m\, c_{\mathrm{He}}}, \tag{41}$$

where m is the mass of the superfluid film, and c_{He} superfluid helium's specific heat capacity. Since the superfluid helium entropy takes the form (*73*):

$$S = \int \frac{c_{\mathrm{He}}}{T} dT, \tag{42}$$

for c_{He} of the form αT^3,

$$S = \int \frac{\alpha T^3}{T} dT = \int \alpha T^2 dT = \frac{\alpha T^3}{3} \simeq \frac{c_{\mathrm{He}}}{3} \tag{43}$$

(Which is indeed what is measured in practice, see ref. (*73*)). Using this, we can re-express Eqs. (40) and (41) as:

$$P_{fp} = \frac{\rho S(T) \hbar\omega}{\rho V c_{\mathrm{He}}(T)} \tag{44}$$

and obtain a simple, temperature-independent expression for the induced fountain pressure resulting from the absorption of a photon of energy $\hbar\omega$:

$$\boxed{P_{\mathrm{fp}} \simeq \frac{\hbar\omega}{3\, V_{\mathrm{He}}}} \tag{45}$$

The goal is therefore to minimize the volume of superfluid covering the resonator, which is attained by reducing the resonator surface area. The above calculation is valid in the regime where:

- The thermal response time of the resonator is slower than that of the superfluid film (which is on the order of a few microseconds at the temperatures considered here), allowing the thermal energy to be transferred to the superfluid film before it is lost to the environment through the resonator's own thermal anchoring.

- The thermal Kapitza conductance at the resonator/superfluid interface is well in excess of the thermal conductance between the helium film and its environment mediated through the vapor pressure. This allows heat to build up in the superfluid film before it is lost to the environment through evaporation. This criterion does not depend strongly on the choice of resonator material as the acoustic impedance mismatch between superfluid helium and most solids commonly used for optical resonator fabrication (e.g., Silica, Silicon, Gallium Arsenide) is of comparable magnitude. This condition is valid for temperatures below ~ 300 mK.

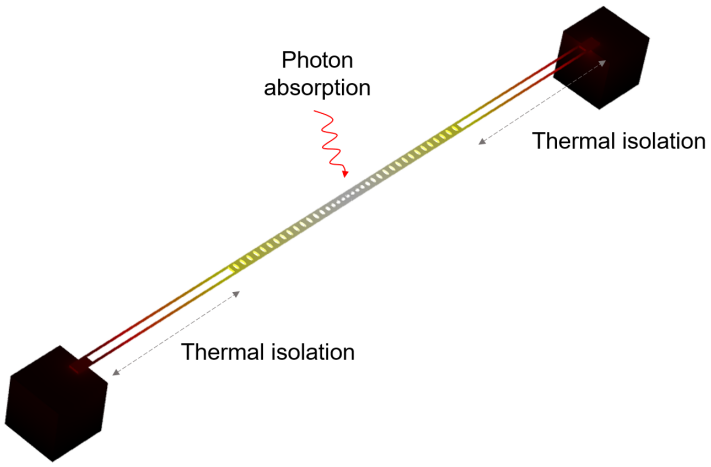

Figure S16: **Silicon 1D photonic crystal architecture.** Long tethers provide thermal isolation from the substrate.

An example architecture satisfying the above conditions is shown in Fig. S16. It consists of a suspended 1D silicon optical crystal cavity, of the kind used in Ref. (*2*). Long and narrow tethers provide sufficient thermal isolation for the heat resulting from optical absorption to be predominantly communicated to the superfluid film. Such a resonator has a optomechanical coupling rate simulated through FEM of $G/2\pi =\sim 5$ GHz/nm (*40*), (meaning that a 1 nm change in thickness of the superfluid film shifts the optical resonance frequency by 5 GHz). Using Eq. 45, we estimate a thickening of the film on the order of 1 nm is achievable per absorbed photon, leading to an optical shift well in excess of the optical resonator linewidth κ (*2*).

8.1 Comparison to radiation pressure per photon

We compare the magnitude of the fountain pressure induced by a photon absorption event (Eq. 45) to the radiation pressure exerted by an intracavity photon. The radiation pressure due to a single photon acting on an element of the superfluid film —which arises due to the change in

electromagnetic energy density due to the presence of the helium—is given by:

$$P_{\mathrm{rad}} = \frac{1}{2}\varepsilon_0 \left(\varepsilon_{\mathrm{sf}} - 1\right) E^2, \tag{46}$$

where the electric field is normalized such that:

$$\frac{1}{2}\iiint \varepsilon_0 \varepsilon_r(\vec{r}) E^2 \mathrm{d}V = \hbar\omega. \tag{47}$$

Making the (strongly) simplifying assumption that the field be essentially localized within the optical resonator (of permittivity ε_r) and of constant magnitude over the mode volume V_{mode}, leads to $E^2 \sim \hbar\omega/(1/2\,\varepsilon_0\,\varepsilon_r\,V_{\mathrm{mode}})$. Combined with Eq. (46), this provides an order of magnitude estimate of achievable the radiation pressure per photon acting on the superfluid film:

$$\boxed{P_{\mathrm{rp}} \simeq \frac{\varepsilon_{\mathrm{sf}} - 1}{\varepsilon_r}\,\frac{\hbar\omega}{V_{\mathrm{mode}}}} \tag{48}$$

Compared to Eq. (45), we note the presence of the prefactor ($\frac{\varepsilon_{\mathrm{sf}}-1}{\varepsilon_r} = 5 \times 10^{-3}$ for a silicon resonator), and the fact that the superfluid volume has been replaced by the (larger) optical mode volume. Combined, these two effects lead to an approximate 3 orders of magnitude reduction compared to the fountain pressure, see Eq. (45).

9 Comparison with thermo-elastic stress in a crystal

The thermal stress σ_{th} arising from a temperature increase ΔT in an isotropic solid of bulk modulus K and thermal expansion coefficient $\alpha = \frac{1}{V}\left(\frac{\partial V}{\partial T}\right)$ is given by:

$$\alpha\Delta T = \frac{\sigma_{\mathrm{th}}}{K}, \tag{49}$$

where for one absorbed photon, ΔT is given by:

$$\Delta T = \frac{\hbar\omega}{\rho V c} \tag{50}$$

This yields a thermal stress per photon of

$$\sigma_{\mathrm{th}} = \frac{\hbar\,\omega\,\alpha\,K}{\rho\,V\,c} \tag{51}$$

This can be re-expressed in simpler form as:

$$\sigma_{\mathrm{th}} = \gamma\frac{\hbar\omega}{V}, \tag{52}$$

where we have introduced the dimensionless Grüneisen parameter $\gamma = \frac{\alpha K}{\rho c}$. For silicon at low temperatures, this takes a value of approximately $\gamma \simeq 0.2$ (*101*), resulting in a thermal stress very close to the superfluid fountain pressure (Eq. (45)). It is thus primarily the compliance of the fluid interface, combined with the engineered ability to collect the thermal energy and operate near the optimal regime $\Omega\tau \sim 1$ which is responsible for the ultralow threshold observed here, and not a fundamentally stronger nature of the fountain pressure force in superfluid helium, making these results broadly applicable to photothermally- and electrothermally-driven systems.

REFERENCES AND NOTES

1. T. Kippenberg, H. Rokhsari, T. Carmon, A. Scherer, K. Vahala, Analysis of radiation-pressure induced mechanical oscillation of an optical microcavity. *Phys. Rev. Lett.* **95**, 033901 (2005).

2. J. Chan, T. P. M. Alegre, A. H. Safavi-Naeini, J. T. Hill, A. Krause, S. Gröblacher, M. Aspelmeyer, O. Painter, Laser cooling of a nanomechanical oscillator into its quantum ground state. *Nature* **478**, 89–92 (2011).

3. A. G. Krause, M. Winger, T. D. Blasius, Q. Lin, O. Painter, A high-resolution microchip optomechanical accelerometer. *Nat. Photonics* **6**, 768–772 (2012).

4. S. Basiri-Esfahani, A. Armin, S. Forstner, W. P. Bowen, Precision ultrasound sensing on a chip. *Nat. Commun.* **10**, 132 (2019).

5. T. Purdy, K. Grutter, K. Srinivasan, J. Taylor, Quantum correlations from a room-temperature optomechanical cavity. *Science* **356**, 1265–1268 (2017).

6. S. Forstner, E. Sheridan, J. Knittel, C. L. Humphreys, G. A. Brawley, H. Rubinsztein-Dunlop, W. P. Bowen, "Ultrasensitive optomechanical magnetometry. *Adv. Mater.* **26**, 6348–6353 (2014).

7. A. H. Safavi-Naeini, S. Gröblacher, J. T. Hill, J. Chan, M. Aspelmeyer, O. Painter, Squeezed light from a silicon micromechanical resonator. *Nature* **500**, 185–189 (2013).

8. R. Riedinger, A. Wallucks, I. Marinković, C. Löschnauer, M. Aspelmeyer, S. Hong, S. Gröblacher, Remote quantum entanglement between two micromechanical oscillators. *Nature* **556**, 473–477 (2018).

9. R. Delaney, M. Urmey, S. Mittal, B. Brubaker, J. Kindem, P. Burns, C. Regal, K. Lehnert, Superconducting-qubit readout via low-backaction electro-optic transduction. *Nature* **606**, 489–493 (2022).

10. W. P. Bowen, G. J. Milburn, Quantum optomechanics, (CRC Press, Boca Raton, ed. 1, 2015).

11. M. Aspelmeyer, T. J. Kippenberg, F. Marquardt, Cavity optomechanics. *Rev. Mod. Phys.* **86**, 1391–1452 (2014).

12. M. Bagheri, M. Poot, M. Li, W. P. H. Pernice, H. X. Tang, Dynamic manipulation of nanomechanical resonators in the high-amplitude regime and non-volatile mechanical memory operation. *Nat. Nanotechnol.* **6**, 726–732 (2011).

13. S. Asakura, F. Oosawa, "On interaction between two bodies immersed in a solution of macromolecules. *J. Chem. Phys.* **22**, 1255–1256 (1954).

14. X. Liu, M. M. Skanata, D. Stein, Entropic cages for trapping dna near a nanopore. *Nat. Commun.* **6**, 6222 (2015).

15. L. G. Treloar, *The physics of rubber elasticity*, (Oxford Univ. Press, 1975).

16. C. H. Metzger, K. Karrai, Cavity cooling of a microlever. *Nature* **432**, 1002–1005 (2004).

17. J. Restrepo, J. Gabelli, C. Ciuti, I. Favero, Classical and quantum theory of photothermal cavity cooling of a mechanical oscillator. *C. R. Phys.* **12**, 860–870 (2011).

18. S. De Liberato, N. Lambert, F. Nori, Quantum noise in photothermal cooling. *Phys. Rev. A* **83**, 033809 (2011).

19. C. Metzger, I. Favero, A. Ortlieb, K. Karrai, Optical self cooling of a deformable Fabry-Perot cavity in the classical limit. *Phys. Rev. B* **78**, 035309 (2008).

20. C. Metzger, M. Ludwig, C. Neuenhahn, A. Ortlieb, I. Favero, K. Karrai, F. Marquardt, Self-induced oscillations in an optomechanical system driven by bolometric backaction. *Phys. Rev. Lett.* **101**, 133903 (2008).

21. A. G. Primo, C. M. Kersul, R. Benevides, N. C. Carvalho, M. Ménard, N. C. Frateschi, P.-L. de Assis, G. S. Wiederhecker, T. P. Mayer Alegre, Accurate modeling and characterization of photothermal forces in optomechanics. *APL Photonics* **6**, 086101 (2021).

22. S. M. Meenehan, J. D. Cohen, S. Gröblacher, J. T. Hill, A. H. Safavi-Naeini, M. Aspelmeyer, O. Painter, Silicon optomechanical crystal resonator at millikelvin temperatures. *Phys. Rev. A* **90**, 011803 (2014).

23. Y. Wen, N. Ares, F. J. Schupp, T. Pei, G. A. D. Briggs, E. A. Laird, A coherent nanomechanical oscillator driven by single-electron tunnelling. *Nat. Phys.*, **16**, 75–82 (2020).

24. C. Urgell, W. Yang, S. L. De Bonis, C. Samanta, M. J. Esplandiu, Q. Dong, Y. Jin, A. Bachtold, Cooling and self-oscillation in a nanotube electromechanical resonator. *Nat. Phys.* **16** 32–37 (2020).

25. K. R. Atkins, Third and fourth sound in liquid Helium II. *Phys. Rev.* **113**, 962–965 (1959).

26. F. M. Ellis, L. Li, Quantum swirling of superfluid helium films. *Phys. Rev. Lett.* **71**, 1577–1580 (1993).

27. G. I. Harris, D. L. McAuslan, E. Sheridan, Y. Sachkou, C. Baker, W. P. Bowen, Laser cooling and control of excitations in superfluid helium. *Nat. Phys.* **12**, 788–793 (2016).

28. Y. P. Sachkou, C. G. Baker, G. I. Harris, O. R. Stockdale, S. Forstner, M. T. Reeves, X. He, D. L. McAuslan, A. S. Bradley, M. J. Davis, W. P. Bowen, Coherent vortex dynamics in a strongly interacting superfluid on a silicon chip. *Science* **366**, 1480–1485 (2019).

29. X. He, G. I. Harris, C. G. Baker, A. Sawadsky, Y. L. Sfendla, Y. P. Sachkou, S. Forstner, W. P. Bowen, Strong optical coupling through superfluid Brillouin lasing. *Nat. Phys.* **16**, 417–421 (2020).

30. M. Douvidzon, S. Maayani, H. Nagar, T. Admon, V. Shuvayev, L. Yang, L. Deych, Y. Roichman, T. Carmon, Toward transformable photonics: Reversible deforming soft cavities, controlling their resonance split and directional emission. *APL Photonics* **6**, 071304 (2021).

31. A. Lee, P. Zhang, Y. Xu, S. Jung, Radiation pressure-induced nonlinearity in a micro-droplet. *Opt. Express* **28**, 12675–12687 (2020).

32. D. McAuslan, G. Harris, C. Baker, Y. Sachkou, X. He, E. Sheridan, W. Bowen, Microphotonic forces from superfluid flow. *Phys. Rev. X* **6**, 021012 (2016).

33. H. London, Thermodynamics of the thermomechanical effect of liquid He II. *Proc. R. Soc. London Series A Math. Phys. Sci.* **171**, 484–496 (1939).

34. C. Enss, S. Hunklinger, *Low-Temperature Physics*, (Springer Science & Business Media, 2005).

35. J. F. Allen, H. Jones, New phenomena connected with heat flow in helium II. *Nature* **141**, 243–244 (1938).

36. M. A. Weilert, D. L. Whitaker, H. J. Maris, G. M. Seidel, Laser levitation of superfluid helium. *J. Low Temp. Phys.* **98**, 17–35 (1995).

37. K. R. Atkins, B. Rosenbaum, H. Seki, Evaporation effects during superflow of liquid helium II. *Phys. Rev.* **113**, 751–754 (1959).

38. F. M. Ellis, H. Luo, Observation of the persistent-current splitting of a third-sound resonator. *Phys. Rev. B* **39**, 2703–2706 (1989).

39. A. M. R. Schechter, R. W. Simmonds, R. E. Packard, J. C. Davis, Observation of ‘third sound’ in superfluid 3He. *Nature* **396**, 554–557 (1998).

40. C. G. Baker, G. I. Harris, D. L. McAuslan, Y. Sachkou, X. He, W. P. Bowen, Theoretical framework for thin film superfluid optomechanics: Towards the quantum regime. *New J. Phys.* **18**, 123025 (2016).

41. M. Poot, K. Y. Fong, M. Bagheri, W. H. P. Pernice, H. X. Tang, Backaction limits on self-sustained optomechanical oscillations. *Phys. Rev. A* **86**, 053826 (2012).

42. A. G. Krause, J. T. Hill, M. Ludwig, A. H. Safavi-Naeini, J. Chan, F. Marquardt, O. Painter, Nonlinear radiation pressure dynamics in an optomechanical crystal. *Phys. Rev. Lett.* **115**, 233601 (2015).

43. D. Cattiaux, X. Zhou, S. Kumar, I. Golokolenov, R. R. Gazizulin, A. Luck, L. M. de Lépinay, M. Sillanpää, A. D. Armour, A. Fefferman, E. Collin, Beyond linear coupling in microwave optomechanics. *Phys. Rev. Res.* **2**, 033480 (2020).

44. H. Choi, M. Heuck, D. Englund, Self-similar nanocavity design with ultrasmall mode volume for single-photon nonlinearities. *Phys. Rev. Lett.* **118**, 223605 (2017).

45. E. Gil-Santos, C. Baker, D. T. Nguyen, W. Hease, C. Gomez, A. Lemaître, S. Ducci, G. Leo, I. Favero, High-frequency nano-optomechanical disk resonators in liquids. *Nat. Nanotechnol.* **10**, 810–816 (2015).

46. P. Kittel, Orbital resupply of liquid helium. *J. Spacecr. Rockets* **23**, 391–396 (1986).

47. S. Kurihara, Large-amplitude quasi-solitons in superfluid films. *J. Physical Soc. Japan* **50**, 3262–3267 (1981).

48. S. Kaminski, L. L. Martin, S. Maayani, T. Carmon, Ripplon laser through stimulated emission mediated by water waves. *Nat. Photonics* **10**, 758–761 (2016).

49. C. Ma, P. Yu, W. Wang, Y. Zhu, F. Lin, J. Wang, Z. Jing, X.-T. Kong, P. Li, A. O. Govorov, D. Liu, H. Xu, Z. Wang, Chiral optofluidics with a plasmonic metasurface using the photothermal effect. *ACS Nano* **15**, 16357–16367 (2021).

50. F. Luo, J. Yang, R. Zhou, Y. Li, T. Luan, Z. Li, J. Wu, Q. Shou, X. Xing, Highly efficient and controllable micromixer through interactions of photothermal multivortices. *Phys. Fluids* **34**, 072011 (2022).

51. R. Zhou, J. Yang, J. Yang, Y. Zhang, F. Luo, Y. Chen, Y. Li, T. Luan, Q. Shou, X. Jiang, X. Hu, J. Wu, C. Liu, H. Zhong, Z. Li, H.-P. Ho, X. Xing, Vortices-interaction-induced microstreaming for the pump-free separation of particles. *Optics Lett.* **46**, 3629–3632 (2021).

52. A. Ashkin,J. M. Dziedzic, Radiation pressure on a free liquid surface. *Phys. Rev. Lett.* **30**, 139–142 (1973).

53. C. Monat, P. Domachuk, B. J. Eggleton, Integrated optofluidics: A new river of light. *Nat. Photonics* **1**, 106–114 (2007).

54. R. Dahan, L. L. Martin, T. Carmon, Droplet optomechanics. *Optica* **3**, 175 (2016).

55. M. L. Douvidzon, S. Maayani, L. L. Martin, T. Carmon, Light and capillary waves propagation in water fibers. *Sci. Rep.* **7**, 16633 (2017).

56. S. Maayani, L. L. Martin, S. Kaminski, T. Carmon, Cavity optocapillaries. *Optica* **3** 552 (2016).

57. I. S. Maksymov, A. D. Greentree, Coupling light and sound: Giant nonlinearities from oscillating bubbles and droplets. *Nanophotonics* **8**, 367–390 (2019).

58. J. Rosenberg, Q. Lin, O. Painter, Static and dynamic wavelength routing via the gradient optical force. *Nat. Photonics* **3**, 478–483 (2009).

59. C. Sun, M. Wade, M. Georgas, S. Lin, L. Alloatti, B. Moss, R. Kumar, A. H. Atabaki, F. Pavanello, J. M. Shainline, J. S. Orcutt, R. J. Ram, M. Popović, V. Stojanović, A 45 nm CMOS-SOI monolithic photonics platform with bit-statistics-based resonant microring thermal tuning. *IEEE J. Solid-State Circuits* **51**, 893–907 (2016).

60. X. He, C. Baker, Y. Sachkou, A. Sawadsky, S. Forstner, Y. Sfendla, and W. Bowen, Phonon Confinement by the Force of Light, in *CLEO Pacific Rim Conference*, (Hong Kong), p. Tu3F.3, OSA, (2018).

61. W. W. Wasserman, R. A. Harrison, G. I. Harris, A. Sawadsky, Y. L. Sfendla, W. P. Bowen, C. G. Baker, Cryogenic and hermetically sealed packaging of photonic chips for optomechanics. *Opt. Express* **30**, 30822–30831 (2022).

62. A. B. Matsko, V. S. Ilchenko, Optical resonators with whispering-gallery modes-part I: Basics. *IEEE J. Sel. Top. Quantum Electronics* **12**, 3–14 (2006).

63. D. R. Tilley, J. Tilley, Superfluidity and superconductivity, (CRC Press, 1990).

64. A. D. Kashkanova, A. B. Shkarin, C. D. Brown, N. E. Flowers-Jacobs, L. Childress, S. W. Hoch, L. Hohmann, K. Ott, J. Reichel, J. G. E. Harris. Superfluid Brillouin optomechanics. *Nat. Phys.* **13**, 74–79 (2017).

65. A. Shkarin, A. Kashkanova, C. Brown, S. Garcia, K. Ott, J. Reichel, J. Harris, Quantum optomechanics in a liquid. *Phys. Rev. Lett.* **122**, 153601 (2019).

66. G. I. Harris, A. Sawadsky, Y. L. Sfendla, W. W. Wasserman, W. P. Bowen, and C. G. Baker, Proposal for a quantum traveling Brillouin resonator. *Opt. Express* **28**, 22450–22461 (2020).

67. F. Souris, X. Rojas, P. Kim, J. Davis Ultralow-dissipation superfluid micromechanical resonator. *Phys. Rev. Appl.* **7**, 044008, (2017).

68. S. Schmid, L. G. Villanueva, M. L. Roukes, *Fundamentals of Nanomechanical Resonators*, (Cham: Springer International Publishing, 2016).

69. M. J. Moloney, Quality factors and conductances in helmholtz resonators. *Am. J. Phys.* **72**, 1035–1039 2004.

70. H. Lamb, *Hydrodynamics*. 1916.

71. Y. L. Sfendla, C. G. Baker, G. I. Harris, L. Tian, R. A. Harrison, W. P. Bowen, Extreme quantum nonlinearity in superfluid thin-film surface waves. *npj Quantum Inf.* **7**, 1–12 (2021).

72. L. Ding, C. Baker, P. Senellart, A. Lemaitre, S. Ducci, G. Leo, I. Favero, High frequency GaAs nano-optomechanical disk resonator. *Phys. Rev. Lett.* **105**, 263903 (2010).

73. R. J. Donnelly, C. F. Barenghi, The observed properties of liquid helium at the saturated vapor pressure. *J. Phys. Chem. Ref. Data Monogr.* **27**, 1217–1274 (1998).

74. G. Sidebotham, *Heat Transfer Modeling*, (Cham: Springer International Publishing, 2015).

75. G. Swift, T. Molinski, W. Lehn, A fundamental approach to transformer thermal modeling. I. Theory and equivalent circuit. *IEEE Trans. Power Deliv.* **16**, 171–175 (2001).

76. J. Altet, A. Rubio, *Thermal Testing of Integrated Circuits*, (Boston, MA: Springer US, 2002).

77. K. J. Kontoleon, Dynamic thermal circuit modelling with distribution of internal solar radiation on varying façade orientations. *Energ. Buildings* **47**, 139–150 (2012).

78. Y. Gan, J. Wang, J. Liang, Z. Huang, M. Hu, Development of thermal equivalent circuit model of heat pipe-based thermal management system for a battery module with cylindrical cells. *Appl. Therm. Eng.* **164**, 114523 (2020).

79. M. P. Zaitlin, A. C. Anderson, "Phonon thermal transport in noncrystalline materials. *Phys. Rev. B* **12**, 4475–4486 (1975).

80. R. C. Zeller, R. O. Pohl, Thermal conductivity and specific heat of noncrystalline solids. *Phys. Rev. B* **4**, 2029–2041 (1971).

81. G. L. Pollack, Kapitza resistance. *Rev. Mod. Phys.*, **41**, 48–81 (1969).

82. E. Long, L. Meyer, Superfluidity and heat transport in the unsaturated helium-II film. *Phys. Rev.* **98**, 1616–1622 (1955).

83. H. Haus, *Waves and fields in optoelectronics.* Prentice-Hall, 1984.

84. D. Browne, Nonlinear effects in the damping of third-sound pulses. *J. Low Temp. Phys.* **57**, 207–226 (1984).

85. K. R. Atkins, C. E. Chase, The velocity of first sound in liquid helium. *Proc. Phys. Soc. Sec. A* **64**, 826–833 (1951).

86. COMSOL Multiphysics Material Library; https://www.comsol.com/material-library.

87. A. K. Raychaudhuri, Origin of the plateau in the low-temperature thermal conductivity of silica. *Phys. Rev. B* **39**, 1927–1931 (1989).

88. J. Rumble, *CRC handbook of chemistry and physics*. (CRC Press LLC, 2017).

89. R. A. Barton, I. R. Storch, V. P. Adiga, R. Sakakibara, B. R. Cipriany, B. Ilic, S. P. Wang, P. Ong, P. L. McEuen, J. M. Parpia, H. G. Craighead, Photothermal self-oscillation and laser cooling of graphene optomechanical systems. *Nano Lett.* **12**, 4681–4686 (2012).

90. R. De Alba, T. S. Abhilash, R. H. Rand, H. G. Craighead, J. M. Parpia, Low-Power Photothermal Self-Oscillation of Bimetallic Nanowires. *Nano Lett.* **17**, 3995–4002 (2017).

91. D. Woolf, P.-C. Hui, E. Iwase, M. Khan, A. W. Rodriguez, P. Deotare, I. Bulu, S. G. Johnson, F. Capasso, M. Loncar, Optomechanical and photothermal interactions in suspended photonic crystal membranes. *Opt. Express* **21**, 7258–7275 (2013).

92. P. E. Allain, B. Guha, C. Baker, D. Parrain, A. Lemaître, G. Leo, I. Favero, Electro-optomechanical modulation instability in a semiconductor resonator. *Phys. Rev. Lett.* **126**, 243901 (2021).

93. L. Mercadé, L. L. Martín, A. Griol, D. Navarro-Urrios, A. Martínez, Microwave oscillator and frequency comb in a silicon optomechanical cavity with a full phononic bandgap. *Nanophotonics* **9**, 3535–3544 (2020).

94. I. Ghorbel, F. Swiadek, R. Zhu, D. Dolfi, G. Lehoucq, A. Martin, G. Moille, L. Morvan, R. Braive, S. Combrié, A. De Rossi, Optomechanical gigahertz oscillator made of a two photon absorption free piezoelectric III/V semiconductor. *APL Photonics* **4**, 116103 (2019).

95. H. Jayakumar, B. Khanaliloo, D. P. Lake, P. E. Barclay, Tunable amplification and cooling of a diamond resonator with a microscope. *Phys. Rev. Appl.* **16**, 014063 (2021).

96. I. S. Grudinin, H. Lee, O. Painter, K. J. Vahala, Phonon laser action in a tunable two-level system. *Phys. Rev. Lett.* **104**, 083901 (2010).

97. W. C. Jiang, X. Lu, J. Zhang, Q. Lin, High-frequency silicon optomechanical oscillator with an ultralow threshold. *Opt. Express* **20**, 15991–15996 (2012).

98. Q. Lin, J. Rosenberg, X. Jiang, K. Vahala, O. Painter, Mechanical oscillation and cooling actuated by the optical gradient force. *Phys. Rev. Lett.* **103**, 103601 (2009).

99. F. M. Ellis, H. Luo, Third sound: Where are the solitons?. *J. Low Temp. Phys.* **89**, 115–124 (1992).

100. F. Pobell, *Matter and methods at low temperatures*, (Springer, ed. 3, 2007).

101. W. B. Gauster, Low-temperature grüneisen parameters for silicon and aluminum. *Phys. Rev. B* **4**, 1288–1296 (1971).